

Effects of Winds on the Optical Properties of Type Ib and Ic Supernova Progenitors

MOO-KEON JUNG ¹, SUNG-CHUL YOON ^{1,2} AND HYUN-JEONG KIM ³

¹*Department of Physics and Astronomy, Seoul National University, Seoul 08826, Korea*

²*SNU Astronomy Research Center, Seoul National University, Seoul 08826, Korea*

³*Korea Astronomy and Space Science Institute, Daejeon 34055, Korea*

(Received September 28, 2021; Revised November 28, 2021; Accepted November 30, 2021)

Submitted to ApJ

ABSTRACT

We investigate the effects of winds on the observational properties of Type Ib and Ic supernova (SN Ib/Ic) progenitors using spectral models constructed with the non-LTE stellar atmospheric code CMFGEN. We consider SN Ib/Ic progenitor models of the final mass range of $2.16 - 9.09 M_{\odot}$ having different surface temperatures and chemical compositions, and calculate the resulting spectra for various wind mass-loss rates and wind terminal velocities. We find that the progenitors having an optically thick wind would become brighter in the optical for a higher mass-loss rate (or a lower wind terminal velocity), because of the formation of the photosphere in the extended wind matter and the contribution from free-free and line emissions from the wind. As a result, for the standard Wolf-Rayet wind mass-loss rate, helium-deficient compact SN Ic progenitors would be brighter in the optical by ~ 3 mag compared to the case without the wind effects. We also find that the color dependence on the photospheric temperature is non-monotonic because of the wind effects. Our results imply that inferring the progenitor mass, bolometric luminosity and effective temperature from the optical observation using the standard stellar evolution model prediction can be misleading. By comparing our fiducial model predictions with the detection limits of the previous SN Ib/Ic progenitor searches, we conclude that a deep search with an optical absolute magnitude larger than ~ -4 is needed to directly identify most of the ordinary SN Ib/Ic progenitors. We discuss implications of our results for the observed SN Ib/Ic progenitor candidates for iPTF13bvn, SN 2019yvr and SN 2017ein.

1. INTRODUCTION

Most supernovae (SNe) except Type Ia SNe are produced by core-collapse in massive stars at the end of their lives. The majority of core-collapse SNe belong to Type II SNe (SNe II) and their progenitors are hydrogen-rich supergiants (e.g., Smith et al. 2011). Type Ib and Ic SNe (SNe Ib/Ic) lack hydrogen lines in their spectra. This implies that their progenitors are single Wolf-Rayet (WR) stars which lost their hydrogen-rich envelopes by stellar wind mass-loss, and/or hydrogen-deficient stars produced in binary systems by interactions with their companion stars (see Yoon 2015, for a review). Recent observational studies indicate that the ejecta mass distribution of SNe Ib/Ic is concentrated in the range of $1 - 4 M_{\odot}$ (e.g., Drout et al. 2011; Cano 2013; Lyman et al. 2014; Taddia et al. 2015). The implied progenitor masses at explosion (i.e., about $2.4 - 5.4 M_{\odot}$) are significantly lower than the observed WR star masses and the predictions of stellar evolution-

ary models of single massive stars (i.e., $M \gtrsim 8 M_{\odot}$; e.g., Hamann et al. 2006; Meynet & Maeder 2005; Eldridge & Vink 2006; Georgy et al. 2012; Yoon 2015; Hamann et al. 2019; Sander et al. 2012, 2019). This favors the binary star scenario for SN Ib/Ic progenitors (e.g., Podsiadlowski et al. 1992; Vanbeveren et al. 1998; Wellstein & Langer 1999; Yoon et al. 2010; Eldridge et al. 2008; Yoon 2015; Yoon et al. 2017).

One of the best methods to study the exact nature of SN progenitors would be to directly identify the progenitor stars in the pre-explosion images. Unlike the SN II progenitors that have been observed as optically bright supergiants (e.g., Smartt 2009, 2015), progenitors of SNe Ib/Ic turn out to be harder to detect. For more than 10 recently observed SNe Ib/Ic, no direct evidence for their progenitors has been found despite fairly deep observations using the *Hubble Space Telescope* (HST) or other ground-based telescopes (e.g., Eldridge et al. 2013; Smith 2014; Smartt 2015; Van Dyk 2017). So far, only

three cases are reported as candidates of SN Ib/Ic progenitors: iPTF13bvn (Type Ib [Cao et al. 2013](#); [Bersten et al. 2014](#); [Eldridge et al. 2015](#)), SN 2019yvr (Type Ib [Kilpatrick et al. 2021](#)), and SN 2017ein (Type Ic [Van Dyk et al. 2018](#); [Kilpatrick et al. 2018](#)), among which only the progenitor of iPTF13bvn has been conclusively identified by its disappearance ([Eldridge & Maund 2016](#); [Folatelli et al. 2016](#)).

This implies that the majority of SN Ib/Ic progenitors are fainter in the optical than the observed WR stars in the local universe. This would be because most SN Ib/Ic progenitors are produced in binary systems and/or because SN Ib/Ic progenitor properties at the pre-SN stage is significantly different from those of observed WR stars due to the evolutionary effects ([Yoon et al. 2012](#)). Several authors make predictions on the optical properties of SN Ib/Ic progenitors using stellar evolution models of single and binary stars under the black body approximation or using detailed non-local thermodynamic equilibrium (non-LTE) stellar atmospheric models ([Yoon et al. 2012](#); [Eldridge et al. 2013](#); [Groh et al. 2013a,b](#); [Kim et al. 2015](#)). One of the important findings in these studies is that the location of the photosphere formed in an optically thick wind is an important factor to determine the optical brightness of a SN Ib/Ic progenitor ([Kim et al. 2015](#)). This means that the uncertain wind mass-loss rate at the pre-SN stage would be critical for the optical properties of SN Ib/Ic progenitors.

In this study, we systematically explore the effects of winds on the optical brightness and spectra of SN Ib/Ic progenitors for a wider parameter space than considered in [Kim et al. \(2015\)](#), in terms of progenitor mass, chemical composition, wind mass-loss rate and wind terminal velocity. For this purpose we use non-LTE stellar atmospheric models calculated with the radiative transfer code CMFGEN ([Hillier & Miller 1998](#); [Hillier et al. 2003](#)). In Section 2, we explain the detailed physical assumptions and SN Ib/Ic progenitor models used in this study. In Section 3, we present our calculation results and discuss observational properties resulting from the various different assumptions of the mass-loss rate and wind terminal velocity. In Section 4, we discuss constraints on the mass-loss rate of SN Ib/Ic progenitors by comparing our models with the detection limits of undetected SN Ib/Ic progenitors provided by previous studies on pre-explosion images. We also discuss the implications of our results for the directly observed SN Ib/Ic progenitor candidates. We conclude and summarize our study in Section 5.

2. MODELS AND PHYSICAL ASSUMPTIONS

2.1. Input Progenitor Models

Most of our progenitor models are based on the study of [Yoon \(2017, hereafter Y17\)](#). These models are constructed by calculating the evolution of pure helium stars at solar metallicity ($Z = 0.02$) using the BEC code (see [Yoon et al. 2010](#), and its references), until the end of core oxygen burning, for 9 different initial helium star masses ($M_{\text{He},i} = 3.9, 4, 6, 8, 10, 12, 15, 20$ and $25 M_{\odot}$). The adopted WR wind mass-loss rate is given by the prescription of [Y17](#). This prescription is based on the empirical mass-loss rates by the Potsdam group ([Hamann et al. 2006](#); [Hainich et al. 2014](#)) for WNe type WR stars (\dot{M}_{WNE}) and by [Tramper et al. \(2016\)](#) for WC/WO type WR stars (\dot{M}_{WC}), respectively, as the following:

$$\dot{M}_{\text{WNE}} = f_{\text{WR}} \left(\frac{L}{L_{\odot}} \right)^{1.18} \left(\frac{Z_{\text{init}}}{Z_{\odot}} \right)^{0.60} 10^{-11.32} \quad (1)$$

for $Y = 1 - Z_{\text{init}}$,

$$\dot{M}_{\text{WC}} = f_{\text{WR}} \left(\frac{L}{L_{\odot}} \right)^{0.83} \left(\frac{Z_{\text{init}}}{Z_{\odot}} \right)^{0.25} Y^{0.85} 10^{-9.20} \quad (2)$$

for $Y < 0.90$,

and

$$\dot{M} = (1 - x)\dot{M}_{\text{WNE}} + x\dot{M}_{\text{WC}} \quad (3)$$

for $0.90 \leq Y < 1 - Z_{\text{init}}$,

where

$$x = (1 - Z_{\text{init}} - Y)/(1 - Z_{\text{init}} - 0.90). \quad (4)$$

Here the mass-loss rate is given in units of $M_{\odot} \text{ yr}^{-1}$, and Y and Z_{init} denote the surface helium mass fraction and the initial metallicity of WR stars, respectively. The wind factor f_{WR} is a free parameter and [Y17](#) suggests $f_{\text{WR}} = 1.58$ to explain the luminosity distribution of WR stars of different types. See [Y17](#) for more details.

We also take two helium-poor SN Ic progenitor models (CO2.16 & CO3.93) from [Yoon et al. \(2019, hereafter Y19\)](#), which are calculated until the pre-SN stage with the MESA code ([Paxton et al. 2011, 2013, 2015, 2018, 2019](#)). For these two models, the standard mass-loss rate of [Nugis & Lamers \(2000, hereafter NL\)](#) until the core helium exhaustion and thereafter an artificially increased mass-loss rate of $\dot{M} = 10^{-4} M_{\odot} \text{ yr}^{-1}$ is adopted. However, because we are interested in exploring the effects of different wind properties on the resulting spectra for a given progenitor structure, the details on how each progenitor model is constructed are not important in this study.

The physical properties of the progenitor models are summarized in Table 1. The model name starting with

‘HE’ refers to the helium-rich models, where the surface mass fraction of helium is $Y = 0.98$ and the integrated helium mass ($m_{\text{HE}} = \int X_{\text{He}} dM_r$) is fairly large ($m_{\text{HE}} \geq 0.88 M_{\odot}$). The model name starting with ‘CO’ refers to the helium-poor models with $Y < 0.5$ and $m_{\text{He}} \leq 0.23 M_{\odot}$. The numbers after HE or CO denote the progenitor masses in units of solar mass at the pre-SN phase. Recent studies indicate that not much helium can be hidden in SNe Ic spectra and here we assume that the HE and CO models represent SN Ib and Ic progenitors, respectively (see Hachinger et al. 2012; Yoon 2017; Yoon et al. 2019; Dessart et al. 2020; Williamson et al. 2021, for related discussions). The considered progenitor masses are $2.91 - 5.05 M_{\odot}$ and $2.16 - 9.09 M_{\odot}$ for helium-rich and helium-poor models, respectively. This can cover most of the SN Ib and Ic progenitor mass range inferred from SN observations (i.e., the SN ejecta masses of $1.0 - 4.0 M_{\odot}$) assuming that the neutron star remnant mass is about $1.4 M_{\odot}$.

We do not consider the rotational line broadening effect because the majority of ordinary SN Ib/Ic progenitors would be slow rotators as they lose a large amount of angular momentum via mass-loss either by winds or binary interactions (see Yoon et al. 2010; Yoon 2015, for a detailed discussion on this issue). We also do not consider the effects of different metallicity. The metallicity can have a variety of effects on the progenitor evolution and structure, the wind mass-loss rate, and the resulting spectra. Our preliminary results indicate that the wind density is the major factor that determines spectral properties for a given progenitor structure and this study covers a wide range of the mass-loss rate (see Section 2.2). Considering the full evolutionary effects of metallicity on the progenitor evolution and structure would be a subject of future work.

Stellar evolution models predict that the surface properties (i.e., luminosity and temperature) of SN Ib/Ic progenitors do not change significantly during the last ~ 10 years before the explosion (see Yoon et al. 2017). However, as discussed in several studies (e.g., Fuller & Ro 2018, etc), energy injection from the neon or oxygen burning convective region during the last evolutionary stage might affect the structure of the outermost layers of progenitor stars and induce a mass-loss enhancement. Full consideration of these effects is beyond the scope of this paper, and here we only implicitly consider possible mass-loss enhancements by assuming various mass-loss rates as explained in Section 2.2.

Figure 1 shows the luminosity-mass ($L - M$) relation and the temperature-luminosity ($T - L$) relation of our

SN Ib/Ic progenitor models. More massive SN Ib/Ic progenitor models by Groh et al. (2013b) and observed Galactic WR stars (Hamann et al. 2019; Sander et al. 2019) are also plotted in the figure for comparison. The comparison models from Groh et al. (2013b) are self-stripped progenitor models that have solar metallicity and initial masses of $25 - 120 M_{\odot}$ and $32 - 120 M_{\odot}$, and final masses of $10.9 - 30.8 M_{\odot}$ and $9.6 - 26.2 M_{\odot}$ for rotating and non-rotating models, respectively. These models are calculated until the end of core carbon burning with the Geneva stellar evolution code (Ekström et al. 2012; Georgy et al. 2012) for which the WR mass-loss rates of NL and Gräfener & Hamann (2008) are used. These models are systematically more massive and luminous than our models, and the final masses are comparable to those of Galactic WR stars. The temperatures of the progenitor models in the right panel of Figure 1 are the hydrostatic surface temperatures (T_{\star}) which are given by the stellar evolution models. However, the temperatures of Galactic WR stars are given by the temperatures at the location where the Rosseland mean optical depth (τ_{ross}) is 20 in stellar atmosphere models (Hamann et al. 2019; Sander et al. 2019), which might not necessarily correspond to the hydrostatic core surface temperatures.

The observed Galactic WR stars in the left panel of Figure 1 follow the theoretical $L - M$ relation for core He-burning WR stars given by Langer (1989). This is simply because the masses of observed WR stars given by Sander et al. (2019) and Hamann et al. (2019) are based on the Langer’s $L - M$ relation. However, all the progenitor models except CO3.93 are several times more luminous than the predictions of the Langer’s $L - M$ relation for a given mass due to a rapid luminosity increase ($\sim 0.2 - 0.3$ dex in logarithmic scale) at the last evolutionary stages compared to the case of helium burning stage (Yoon et al. 2012; Groh et al. 2013b; Yoon 2017). This implies that the evolutionary effects should be properly considered when inferring WR star masses from their luminosities.

2.2. Atmospheric Modeling

To compute our model spectra of SN Ib/Ic progenitors, we use the non-LTE atmospheric radiative transfer code CMFGEN (Hillier & Miller 1998; Hillier et al. 2003). The CMFGEN code determines the temperature distribution of the expanding atmosphere by solving the statistical and radiative equilibrium equations, and computes line and continuum formation under the assumption of the spherical symmetric geometry (Hillier 1990).

Table 1. Input Physical Parameters of SN Ib/Ic Progenitor Models

Name	$M_{\text{He},i}$	M	$\log L$	T_*	R_*	\dot{M}_{fid}	$v_{\infty,\text{fid}}$	m_{He}	Y	$\log X_{\text{C}}$	$\log X_{\text{N}}$	$\log X_{\text{O}}$
	(M_{\odot})	(M_{\odot})	(L_{\odot})	(K)	(R_{\odot})	($M_{\odot} \text{ yr}^{-1}$)	(km s^{-1})	(M_{\odot})				
HE2.91	3.9	2.91	4.66	16850	25.04	2.37e-06	184.49	1.06	0.98	-3.31	-1.82	-3.44
HE2.97	4.0	2.97	4.68	19060	19.98	2.51e-06	206.87	1.07	0.98	-3.31	-1.82	-3.44
HE4.09	6.0	4.09	4.97	36310	7.67	5.50e-06	335.08	1.11	0.98	-3.66	-1.86	-3.09
HE5.05	8.0	5.05	5.11	47960	5.22	8.13e-06	415.33	0.88	0.98	-3.69	-1.86	-3.08
CO5.18	10.0	5.18	5.12	95080	1.34	1.55e-05	728.36	0.23	0.42	-0.33	-	-1.10
CO5.50	12.0	5.50	5.18	117300	0.94	1.26e-05	942.76	0.17	0.21	-0.27	-	-0.65
CO6.17	15.0	6.17	5.22	133300	0.76	1.41e-05	1157.21	0.20	0.23	-0.27	-	-0.68
CO7.50	20.0	7.50	5.33	172800	0.52	1.70e-05	1715.16	0.18	0.21	-0.28	-	-0.62
CO9.09	25.0	9.09	5.43	191700	0.47	1.95e-05	2171.91	0.16	0.19	-0.29	-	-0.56
CO2.16		2.16	4.40	198900	0.13	3.07e-06	414.08	0.06	0.31	-0.27	-	-0.89
CO3.93		3.93	4.26	76630	0.77	3.25e-06	798.00	0.10	0.49	-0.36	-	-1.19

NOTE—Input model parameters of SN Ib/Ic progenitors which are given by the stellar evolution codes (BEC or MESA). Upper nine models are based on Y17, and the other two models are from Y19. From left to right, each column has the meaning of

- $M_{\text{He},i}$: the initial mass of the He star at the beginning of the stellar evolution code,
- M : the SN progenitor mass after finishing the stellar evolution code,
- L : the total bolometric luminosity of the progenitor,
- T_* , R_* : the hydrostatic surface temperature and radius (without correcting the optical depth effects from the wind),
- \dot{M}_{fid} : the mass-loss rate calculated with the Y17 prescription for the given surface properties of the progenitor model,
- $v_{\infty,\text{fid}}$: the wind terminal velocity calculated with the equations 6 & 7,
- m_{He} : the integrated helium mass,
- Y , X_{C} , X_{N} , X_{O} : the surface mass fraction of helium, carbon, nitrogen and oxygen of the progenitor.

While the CMFGEN code computes the radiative transfer self-consistently, it does not solve the momentum equation and we need to specify the hydrodynamic structure of the wind. We assume the standard β law for the wind velocity profile with $\beta = 1$, which is given by

$$v(r) = v_0 + (v_{\infty} - v_0) \left(1 - \frac{R_*}{r}\right)^{\beta}, \quad (5)$$

where v_0 and v_{∞} denote the velocity at the hydrostatic stellar surface and the terminal velocity, respectively, and R_* means the hydrostatic stellar surface radius (Lamers & Cassinelli 1999).

We take the mass-loss rate given by Y17 with $f_{\text{WR}} = 1.58$ (see above) as our fiducial mass-loss rate \dot{M}_{fid} for all our progenitor models (see Table 1). We determine the wind terminal velocities of our fiducial models ($v_{\infty,\text{fid}}$) by the equations for WN and WC stars from NL as the following. For WN stars,

$$\log v_{\infty}/v_{\text{esc}}(\text{core}) = 0.61 - 0.13(\pm 0.09) \log L + 0.30(\pm 0.77) \log Y. \quad (6)$$

For WC stars,

$$\log v_{\infty}/v_{\text{esc}}(\text{core}) = -2.37 + 0.43(\pm 0.13) \log L - 0.07(\pm 0.27) \log Z. \quad (7)$$

The escape velocity at the stellar surface is defined as

$$v_{\text{esc}}(\text{core}) = \sqrt{\frac{2GM(1 - \Gamma_e)}{R_*}}. \quad (8)$$

The Eddington factor Γ_e is defined as

$$\Gamma_e = 7.66 \times 10^{-5} \sigma_e (L/L_{\odot}) / (M/M_{\odot}), \quad (9)$$

where σ_e denotes the electron scattering opacity (see NL). When calculating the wind terminal velocity, we assume the HE models as WN stars and the CO models as WC stars. The spectra of the most massive CO model (CO9.09) might look like a WO star rather than a WC star, depending on the adopted wind parameters (see Section 3.1). The observed WO stars have a very high wind terminal velocity of $\sim 5000 \text{ km s}^{-1}$ (Drew et al. 2004; Sander et al. 2012). However, we consider various mass-loss rates ($\dot{M}_{\text{fid}} \times 0.1, 0.5, 2.0, 5.0$ and 10.0) and wind terminal velocities ($v_{\infty,\text{fid}} \times 0.1, 0.5, 2.0,$ and 3.0)

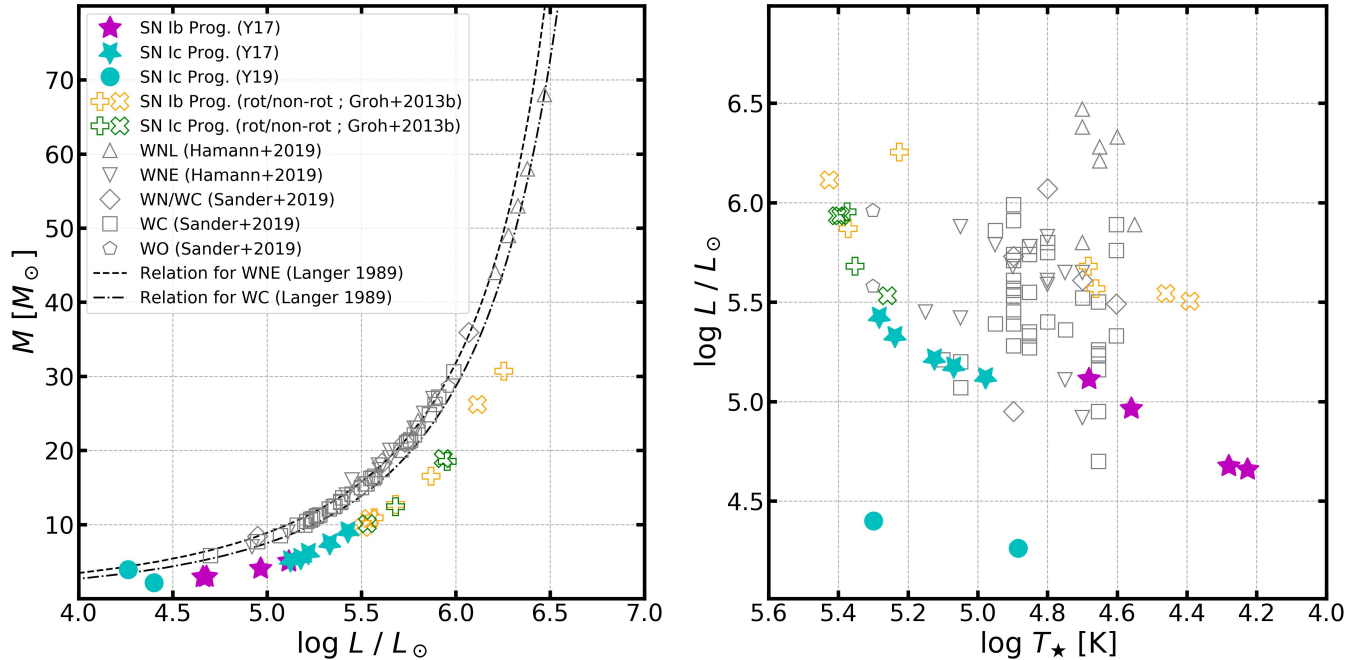


Figure 1. The luminosity-mass relation (left) and the temperature-luminosity relation (right) of SN Ib/IC progenitor models. The upright and inverted stars denote the SN Ib and Ic progenitor models of Y17. The SN Ic progenitor models of Y19 are denoted by filled circles. The rotating and non-rotating self-stripped SN Ib/IC progenitor models of Groh et al. (2013b) are presented by plus and X markers for comparison. The observed Galactic WR stars from Sander et al. (2019) and Hamann et al. (2019) are presented by polygons. The dashed and dashed-dotted lines show the luminosity-mass relation for WNE and WC ($Y = 0.3$) stars given by Langer (1989).

in our model grid, and a wind terminal velocity of 5000 km s^{-1} is covered within our parameter space. The assumed volume filling factor f_c of the wind matter, which is the inverse of the wind clumping factor, is 0.1. Note that WR spectra would look similar for a given value of $\dot{M}/\sqrt{f_c}v_{\infty}$ (see Hamann & Koesterke 1998, etc).

We take some WR and O type star models provided by the CMFGEN code as our initial trial models, which have the most similar temperature and surface gravity values to those of our input models. We first obtain the fiducial models with the fiducial mass-loss rate (\dot{M}_{fid}) and the fiducial wind terminal velocity ($v_{\infty, \text{fid}}$), which are determined with L , R_{\star} and chemical abundances of each model (see Table 1). Then we calculate other models with various mass-loss rates or wind terminal velocities from the fiducial models.

3. RESULTS OF THE ATMOSPHERIC MODELS

3.1. The fiducial models

In Table 2, we present the CMFGEN output results of our fiducial models. The photospheric values of the temperature and radius are obtained at the photosphere defined by the Rosseland mean opacity, which is located in the wind matter above the hydrostatic surface. The corresponding absolute optical magnitudes of different

HST Wide Field Planetary Camera 2 (WFPC2) filters are also given in the table. We choose the *HST*/WFPC2 filter system to compare the progenitor model magnitudes with the progenitor detection limits of previous searches (see Section 4.1). Given that the instrument was replaced with the *HST* Wide Field Camera 3 (WFC3) in 2009, we also provide the progenitor magnitudes of the *HST*/WFC3 filter system in Appendix A to be compared with recent and future data. We find that the magnitude difference between the two filter systems is minor for HE models but significant for CO models (i.e., up to ~ 1 mag).

We present four examples of spectral energy distributions (SEDs) in Figure 2. Here, the HE2.91 and CO9.09 progenitor models have the lowest and highest surface temperatures among our input models from Y17. The HE5.05 and CO5.18 progenitor models have a similar mass and bolometric luminosity, but very different surface compositions and hydrostatic surface temperatures (see Table 1).

Note that a strong line blanketing in the ultra-violet wavelength region and many emission lines in the optical region are observed in the full spectra of the models.

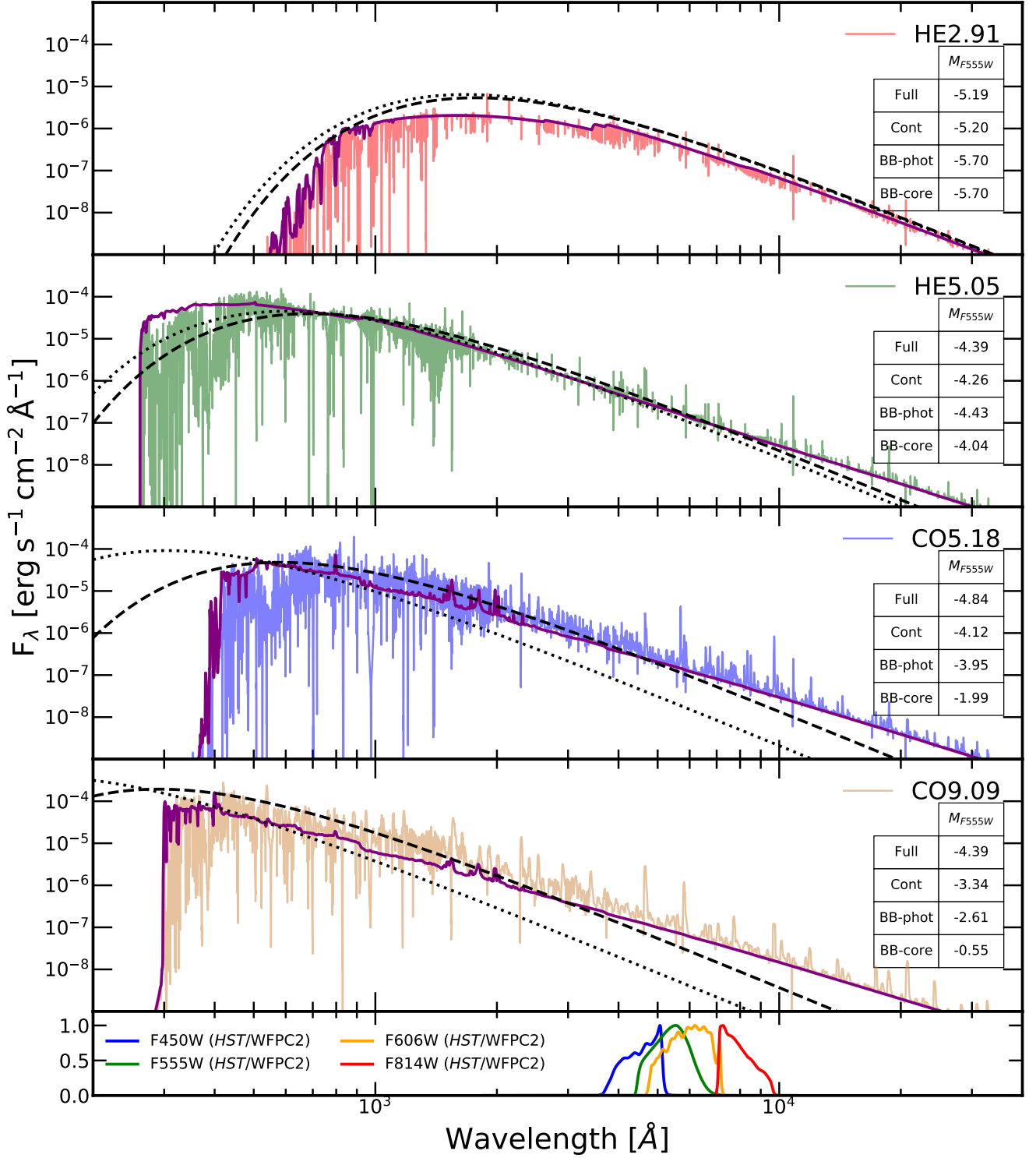


Figure 2. Spectral energy distributions from different SN Ib/Ic progenitor models (HE2.91, HE5.05, CO5.18 and CO9.09). Continuum fluxes are presented by the purple line. The black body fluxes at the photosphere (BB-phot) and the hydrostatic core (BB-core) are plotted with the dashed and dotted lines, respectively. Transmission curves of $F450W$, $F555W$, $F606W$ and $F814W$ filters in *HST* Wide Field and Planetary Camera 2 (WFPC2) are plotted in the lowest panel. The absolute $F555W$ filter magnitude (M_{F555W}) of each case is presented in the inner table. All fluxes are scaled to a distance of 10 pc.

Table 2. CMFGEN output parameters and optical magnitudes of SN Ib/Ic progenitors

Name	T_{eff}	R_{phot}	M_{F450W}	M_{F555W}	M_{F606W}	M_{F814W}
	(K)	(R_{\odot})	(mag)	(mag)	(mag)	(mag)
HE2.91	16330	26.65	-5.26	-5.19	-5.19	-5.16
HE2.97	18390	21.46	-5.11	-5.01	-5.00	-4.92
HE4.09	34730	8.38	-4.73	-4.54	-4.48	-4.31
HE5.05	41910	6.83	-4.56	-4.39	-4.34	-4.29
CO5.18	49850	4.88	-4.83	-4.84	-4.76	-4.74
CO5.50	68200	2.78	-4.54	-4.42	-4.24	-4.27
CO6.17	73450	2.51	-4.59	-4.46	-4.22	-4.22
CO7.50	89770	1.91	-4.53	-4.52	-4.25	-4.11
CO9.09	99710	1.73	-4.42	-4.39	-4.10	-3.97
CO2.16	74890	0.94	-2.66	-2.55	-2.40	-2.45
CO3.93	48080	1.95	-2.83	-2.81	-2.78	-2.78

NOTE—The meaning of each model name is same as that in Table 1. From left to right, each column has the meaning of
 $-T_{\text{eff}}$, R_{phot} : the effective temperature and the photospheric radius defined at the Rosseland optical depth $\tau_{\text{Ross}} = 2/3$.
 $-M_{F450W, F555W, F606W, F814W}$: the absolute magnitude in $F450W$, $F555W$, $F606W$ and $F814W$ filters in *HST*/WFPC2.

For comparison, we also plot the continuum flux given by CMFGEN, the black body flux at the photosphere (BB-phot) and the black body flux at the hydrostatic stellar surface (BB-core) of each model together. The difference between the black body flux at the photosphere and the hydrostatic stellar surface is relatively large for the CO models compared to the HE models. This is because the CO models are more compact and have a denser wind, leading to a significant lifting-up of the photosphere compared to the HE models (see Tables 1 and 2). As a result, the CO models with BB-phot cases are significantly brighter in the optical than the corresponding BB-core case, and the full spectra cases are even brighter than BB-phot case (e.g., *HST*/WFPC2 F_{555W} filter magnitudes $M_{F_{555W}} = -4.39$ and $M_{F_{555W}} = -0.55$ for the full spectrum and BB-core cases of CO9.09, respectively; see Figure 2), while the differences are relatively small for the HE models.

Among the fiducial models in Figure 2, the full spectrum model of HE2.91 is fainter than the corresponding BB-core and BB-phot cases in the optical, in contrast to the other cases. This progenitor model has a surface helium mass fraction of $Y = 0.98$ and an effective temperature of $T_{\text{eff}} = 16330$ K. The helium-rich and hydrogen-free property causes the He bound-free discontinuity at 3422 \AA , which corresponds to the ionization from the 2^3P state of He I. This discontinuity is also shown in previous spectral models and observations of He-rich stars having a similar temperature range ($T_{\text{eff}} \sim 16000 - 24000$ K) (e.g., Popper 1947; Hunger & Klinglesmith 1969; Rosendhal & Schmidt 1973; Cidale et al. 2007). This continuous helium absorption makes the full spectrum brightness fainter than the BB-core and BB-phot brightness in the optical for HE2.91 model. The same phenomenon is also found for the HE2.97 model that has a similar surface temperature to the HE2.91 model.

In Figure 2, we find that the continuum flux exceeds the BB-phot flux in a relatively long wavelength range for the HE5.05, CO5.18 and CO9.09 models. For example, such an excess is found for $\lambda > 5000 \text{ \AA}$ in the CO5.18 model. This excess is due to the free-free emission from the ionized stellar winds, and can significantly affect optical magnitudes, especially in red filters.

In Figure 3, we show $M_{F_{555W}}$ of our fiducial models calculated with the full spectra (black markers), compared to the continuum flux (magenta), BB-phot (green) and BB-core cases (cyan). It is clearly seen that for the CO models $\log T_{\star} [\text{K}] > 4.8$, the optical brightness becomes significantly higher when the full SEDs are taken into account than the BB-core case. This is mainly be-

cause of the effect of lifting-up of the photosphere with an optically thick wind, as discussed above.

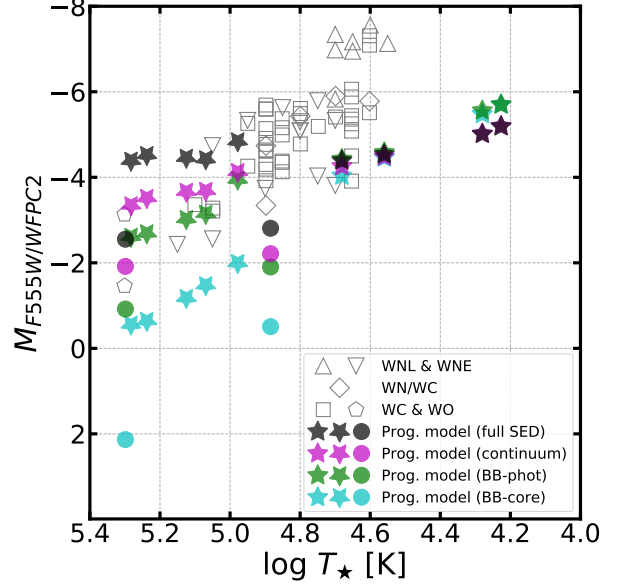


Figure 3. Absolute magnitudes of SN Ib/Ic progenitors in the F_{555W} (*HST*/WFPC2) filter. The upright and inverted stars denote the HE and CO progenitor models from Y17, respectively. The CO progenitor models from Y19 are denoted by filled circles. Different colors give the optical magnitudes calculated with full SED, continuum flux, black body flux at the photosphere (BB-phot) and the hydrostatic surface (BB-core) as indicated by the labels. Galactic WR star samples from Sander et al. (2019) and Hamann et al. (2019) are plotted together for comparison (Note that the temperatures of Galactic WR stars are calculated at the radius of $\tau_{\text{ross}} = 20$ and the absolute magnitudes of them are obtained in the Smith v filter ($\lambda_{\text{peak}} = 5160 \text{ \AA}$; Smith (1968a)).).

On the other hand, the magnitudes $M_{F_{555W}}$ of the HE models $\log T_{\star} [\text{K}] < 4.8$ do not change much for different cases of full SED, continuum flux, BB-phot, and BB-core. This is because the HE models have a relatively large radius at the hydrostatic surface and the resulting wind density with \dot{M}_{fid} is not high enough to cause a significant lifting-up effect of the photosphere. For the cases of HE2.91 and HE2.97, continuum luminosity is fainter than BB-core luminosity in the optical due to the continuous He absorption as discussed above.

Figure 4 shows the optical spectra normalized by continuum, which can be used for WR classification (Smith 1968b). In HE2.91, most lines appear as absorption lines except for a few P Cygni profiles of He I. In HE5.05, many P Cygni profiles and emission lines are found. HE5.05 may be classified as WN7-8 due to its strong N III $\lambda 4634$ emission line, and the similar strength between He I and He II lines. In CO5.18, a strong C III

$\lambda 5696$ emission line and a relatively weak C IV $\lambda 5805$ emission line are seen. In CO9.09, a strong C IV line is seen but the C III $\lambda 5696$ line is absent. The O IV and O V emission lines are also found. CO5.18 and CO9.09 may correspond to WC8-10 and WC4/WO4 stars respectively. Normalized spectra of all the models with the fiducial mass-loss rate are presented in Appendix B. The CO3.93 and CO2.16 models of Y19 show very similar normalized spectra to those of CO5.18 and CO5.50, respectively.

The effect of emission lines on the optical brightness can be observed when we compare the full SED flux and the continuum flux. The optical magnitudes of M_{F555W} calculated with them are also summarized in the inner tables in Figure 2. The HE models have a similar M_{F555W} for full spectra and continuum. For the CO models, however, the optical brightness with full spectra are significantly brighter than those with continuum. This implies that the effect of emission lines is more important for SN Ic progenitors than SN Ib progenitors. The degree of this brightening by emission lines varies non-linearly with the wind density and the effective temperature, as discussed in Section 3.2.

Note also that the optical brightness (M_{F450W} , M_{F555W} , M_{F606W} and M_{F814W}) of the CO models are similar or somewhat lower than those of the HE models, although the bolometric luminosities of most CO models are systematically higher than the HE models (Table 1, 2 and the right panel of Figure 1). This qualitatively confirms the conclusions of Yoon et al. (2012), who argued that SN Ic progenitors would be fainter than SN Ib progenitors. However, Yoon et al. (2012) adopt the black body approximation with the hydrostatic surface temperature (i.e., BB-core case) and they significantly underestimate the optical brightness of SN Ic progenitors.

In Figure 3, we find that our fiducial models are systematically fainter than Galactic WR stars. This is mainly because our models have a lower mass and bolometric luminosity than the Galactic WR stars, on average. However, the lowest mass HE models (HE2.91 and HE2.97) have optical magnitudes comparable to WR stars of $M \simeq 20 M_{\odot}$ (i.e., Smith v filter magnitude $M_v \simeq -5.2$), despite their low bolometric luminosities (see Figure 1). This is because these models have a large radius ($R_{\star} \simeq 20 - 25 R_{\odot}$) and a low surface temperature ($T_{\star} \simeq 17000 - 19000$ K), compared to those of Galactic WR stars. These models are also brightest in the optical among our models, implying that relatively low-mass helium star progenitors ($M \lesssim 3.0 M_{\odot}$) would be relatively easy to detect in the visual wavelength range, compared to more massive SN Ib/Ic progenitors (Yoon

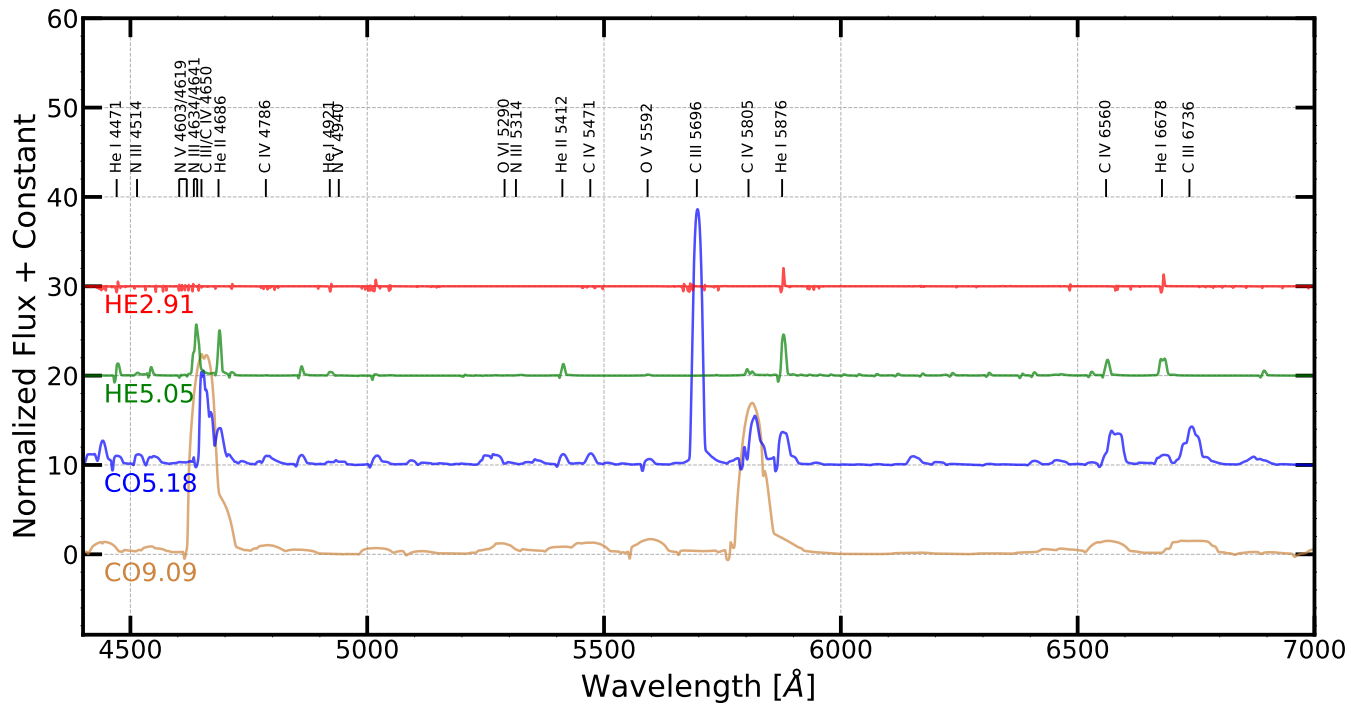
et al. 2012; Kim et al. 2015; Folatelli et al. 2016; Eldridge & Maund 2016; Yoon 2017).

3.2. Effects of the mass-loss rate and the wind terminal velocity

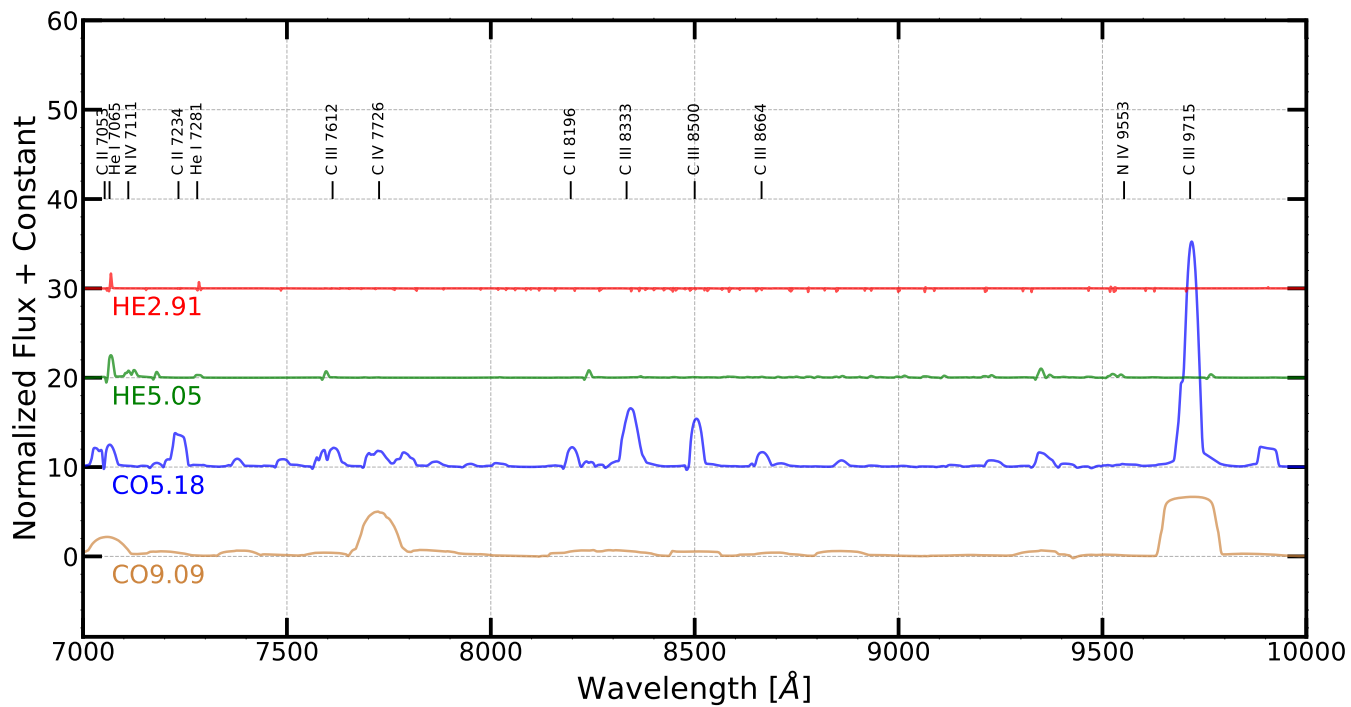
As discussed above in Section 3.1, the effects of winds on the optical brightness can be significant. However, the mass-loss rate of SN Ib/Ic progenitors at the pre-SN stage is uncertain and might be different from the mass-loss rate of the observed WR stars which would be mostly at core helium burning stage (cf. Yoon 2017).

We present the result of a parameter study with various mass-loss rates ($\dot{M} = 0.1 \dot{M}_{\text{fid}} - 10 \dot{M}_{\text{fid}}$) and wind terminal velocities ($v_{\infty} = 0.1 v_{\infty, \text{fid}} - 3 v_{\infty, \text{fid}}$) in Figure 5. Increasing the mass-loss rate or decreasing the wind terminal velocity implies a denser wind, which leads to a lower effective temperature and a higher brightness in the optical. As seen in the figure, this effect is more prominent in the CO models (i.e., the models with $\log T_{\star} [\text{K}] > 4.8$ in the figure) than the HE models ($\log T_{\star} [\text{K}] < 4.8$ in the figure). For example, an increase in \dot{M} by a factor of 100 can lead to a 4 – 6 mag difference in M_{F555W} for CO models. This dependency of the optical brightness on the mass-loss rate allows us to find a constraint on the mass-loss rate of some SN Ib/Ic progenitors as discussed below (Section 4). Normalized optical spectra of HE5.05 and CO5.18 with various mass-loss rates are presented in Appendix C. The figures show that optical properties and emission lines of CO5.18 are more sensitively dependent on the adopted mass-loss rate than the corresponding HE5.05 case. This is because the CO5.18 progenitor model is much more compact than HE5.05, making the effects of winds on the spectra more important.

In Figure 6, we present the color of the models for various wind mass-loss rates as functions of the hydrostatic surface temperature and the effective temperature. The color would be a monotonic function of the effective temperature if the stars emitted black body radiation, as shown in the lower right panel of the figure. However, the continuum can be greatly affected by free-free emission as discussed above. The difference between middle and right panels in the figure shows the effect of free-free emission. The continuum flux colors of the CO models ($\log T_{\star} [\text{K}] > 4.8$ in the figure) are redder than the HE models ($\log T_{\star} [\text{K}] < 4.8$ in the figure) for the fiducial mass-loss rate, despite their higher T_{eff} . For a given T_{eff} , the continuum color is redder for a higher mass-loss rate due to the higher wind density and stronger free-free emission. The same result can also be found in Kim et al. (2015).



(a)



(b)

Figure 4. Normalized optical spectra of some selected SN Ib/Ic progenitor models in the wavelength ranges (a) $4400 \text{ \AA} \leq \lambda \leq 7000 \text{ \AA}$ and (b) $7000 \text{ \AA} \leq \lambda \leq 10000 \text{ \AA}$, which are correspond to the wavelength range of *F555W* and *F814W* filters (*HST*/*WFPC2*), respectively.

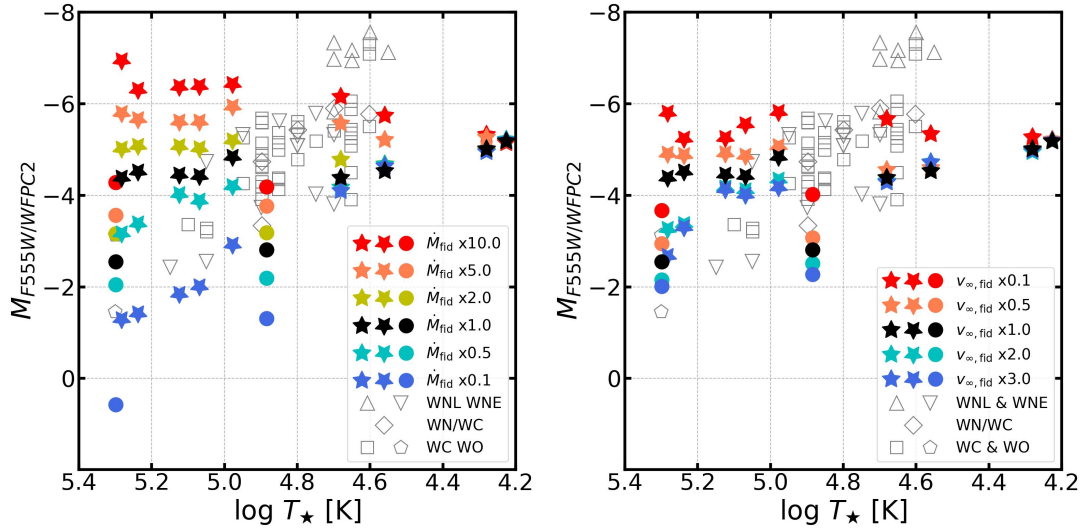


Figure 5. F_{555W} ($HST/WFPC2$) filter magnitudes of SN Ib/Ic progenitors with various mass-loss rates (left) and wind terminal velocities (right). The upright and inverted stars denote the HE and CO progenitor models from Y17, respectively. The CO progenitor models from Y19 are presented with filled circles. Smith v filter ($\lambda_{\text{peak}} = 5160\text{\AA}$) magnitudes of Galactic WR stars are plotted together for comparison (Sander et al. 2019; Hamann et al. 2019). Each color of the markers gives the adopted mass-loss rate and the wind terminal velocity as indicated by the labels.

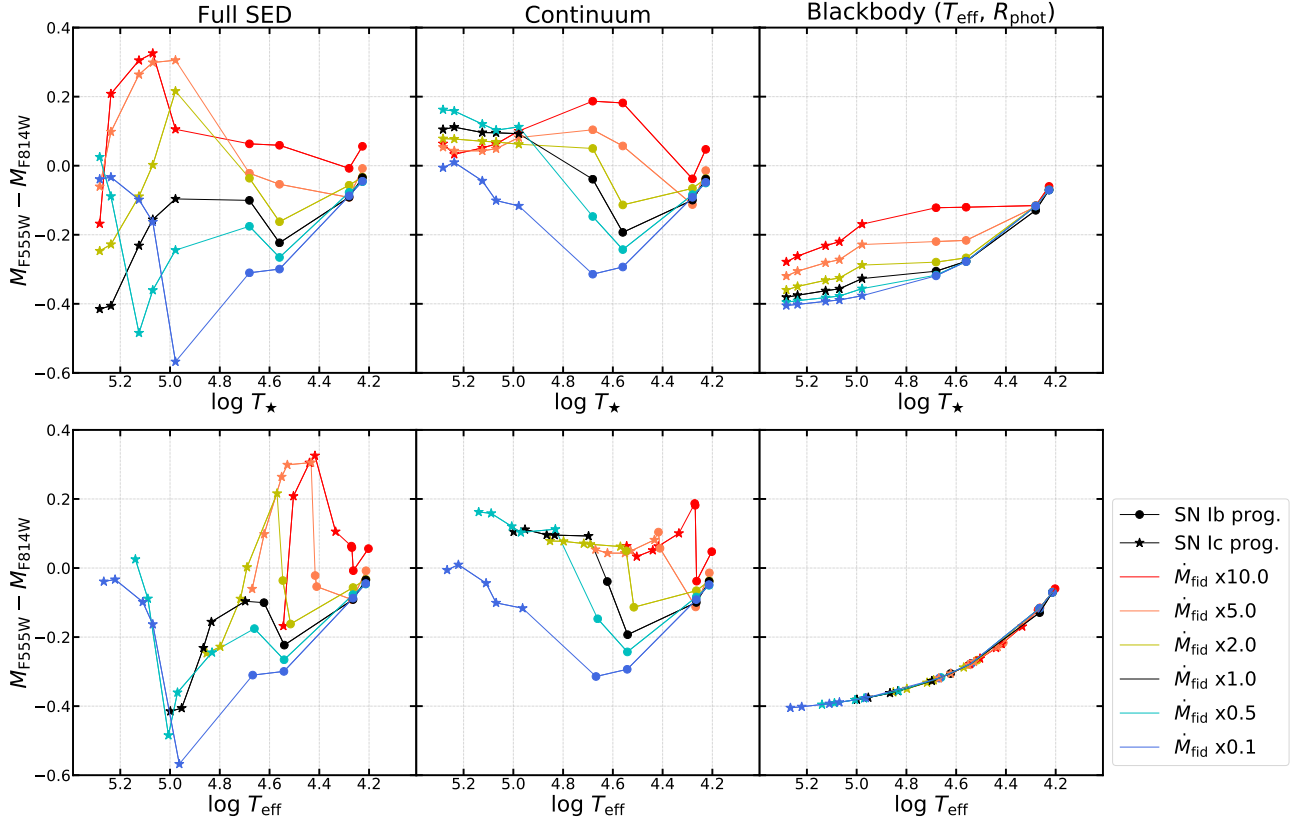


Figure 6. Temperature-color relations for the SN Ib/Ic progenitor models from Y17 (see Table 1, 2 and 5). The left panels show the $M_{F555W} - M_{F814W}$ (*HST*/*WFPC2*) colors calculated with full SEDs. The middle and right panels show the same colors calculated only with the continuum and black body fluxes at the photosphere, respectively. The circle and star markers denote SN Ib and Ic progenitor models, respectively. The color gives the adopted mass-loss rate as indicated by the labels. \dot{M}_{fid} means the fiducial mass-loss rate used in this paper.

Moreover, emission lines from the wind matter can also play an important role in determining the optical brightness in a specific filter. The difference between left and middle panels of Figure 6 shows the effect of emission lines. In many of our models with the fiducial mass-loss rate, more strong emission lines are found in the spectral range of the $F555W$ filter than in the $F814W$ filter range (see Figure 4 and figures in Appendix), and it generally makes the color of the fiducial models with full SED bluer than the continuum color. The CO5.50, CO6.17 and CO7.50 models with a very high mass-loss rate (i.e., 5 and 10 times the fiducial value), however, have a redder color with the full spectrum compared to the continuum color. This is because of strong C II/C III emission lines in the $F814W$ filter wavelength range in these models.

In short, the optical magnitude variation of SN Ib/Ic progenitors according to the wind density can be up to ~ 6 mag for our considered parameter space (see Figure 5). The corresponding color change according to the effective temperature and the wind density is highly non-monotonic and the progenitor color in terms

of $M_{F555W} - M_{F814W}$ can be significantly redder (up to ~ 0.7 mag) or bluer (up to ~ 0.2 mag) depending on the progenitor structure and mass-loss rate, compared to the corresponding prediction under the black body approximation (see Figure 6). This result indicates that prediction of the optical brightness and color of SN Ib/Ic progenitors using the black body approximation can lead to a significant error, and the effects of winds need to be properly considered to infer/constrain the progenitor properties from observations.

3.3. Comparison with the Analytic Prediction

De Loore et al. (1982) present a simple analytic prediction for the photospheric radius and the effective temperature of a WR star having an optically thick wind. For example, assuming a constant opacity κ , $\beta = 2$ and $v(r = R_*) = 0$ in the standard β -low wind velocity profile, the photospheric radius can be given as follows (Langer 1989):

$$R_{\text{phot}} = R_* + \frac{3\kappa|\dot{M}|}{8\pi v_\infty}. \quad (10)$$

For $\beta = 1$ as assumed in this study, we get

$$R_{\text{phot}} = R_{\star} \left[1 - \exp \left(\frac{8\pi R_{\star} v_{\infty}}{3\kappa |\dot{M}|} \right) \right]^{-1}. \quad (11)$$

With this R_{phot} , we can compute T_{eff} from the Stefan-Boltzmann law (i.e., $T_{\text{eff}} = T_{\star} (R_{\star}/R_{\text{phot}})^{1/2}$).

In Figure 7, we compare these analytically obtained R_{phot} and T_{eff} for $\beta = 1$ with the CMFGEN results. We find that the two cases relatively well agree within 20 per cent, implying that the analytical prescription for R_{phot} and T_{eff} would be useful for a rough guess, particularly for SN Ib progenitors. The caveat is that any prediction on optical magnitudes and color from this T_{eff} under the black body assumption could result in a significant error, as discussed above in Sections 3.1 and 3.2.

4. IMPLICATIONS FOR SUPERNOVA PROGENITORS

4.1. Comparison with the detection limits of pre-explosion images

There are only a limited number of candidates for SN Ib/Ic progenitors: SN Ib progenitor candidates for iPTF13bvn (Cao et al. 2013) and SN 2019yvr (Kilpatrick et al. 2021), and SN Ic progenitor candidate for SN 2017ein (Van Dyk et al. 2018; Kilpatrick et al. 2018). In the cases of no direct identification, we can get the detection limits from the pre-explosion images. Eldridge et al. (2013) report the detection limits for 12 SN Ib/Ic progenitors from the observations (See also Smartt (2015) and Van Dyk (2017)). We add a detection limit of the pre-explosion image of SN Ic 2020oi (Gagliano et al. 2021). The detection limit is -4.2 mag in $F555W$ filter ($HST/WFC3$) and obtained with the 3σ limit of the pre-explosion image. In Figure 8, we present the detection limits in various filters. We compare the absolute magnitudes of our SN Ib/Ic progenitor models calculated with the same filter system. Note that the host galaxy extinction has not been considered in some of this sample (Eldridge et al. 2013; Gagliano et al. 2021), in which case the detection limits might be lower than the given values. Even for the case where the host galaxy extinction was inferred, its uncertainty can be significant, which might also affect the estimated detection limits.

In principle, we can roughly infer the upper limit of the mass-loss rate of these non-detected progenitors because the optical brightness becomes systematically higher for a higher mass-loss rate, in particular for SN Ic progenitors. We find that the observational detection limits except for SN 2002ap are located above the CO2.16/CO3.93 model predictions (circle symbols) with $\dot{M}_{\text{fid}} \times 10.0$ in Figure 8. When compared to the relatively

massive CO model predictions ($M > 5.0 M_{\odot}$, inverted star symbols), the observational detection limits except for 3 cases (SN 2002ap, SN 2010br and SN 2020oi) are located above the model predictions with $\dot{M}_{\text{fid}} \times 2.0$. For SN 2010br and the SN 2020oi, the mass-loss rate of the progenitor would not exceed twice the fiducial mass-loss rate if their final masses were relatively high ($M \gtrsim 5 M_{\odot}$), while the upper limit of the mass-loss rate of the progenitor would be higher than $\dot{M}_{\text{fid}} \times 10$ if their final masses were relatively low ($M \lesssim 4 M_{\odot}$). The detection limit of SN 2002ap is -4.4 mag in Johnson-B filter, which is larger than the fiducial model predictions of relatively massive CO progenitors ($M \gtrsim 5 M_{\odot}$) and smaller than the CO2.16/CO3.93 model cases. This implies either that the SN 2002ap progenitor did not have a strong wind or that the progenitor final mass was relatively low ($M \lesssim 4 M_{\odot}$). The observationally inferred ejecta mass of SN 2002ap is about $2.5 M_{\odot}$ (Mazzali et al. 2007), which is consistent with the latter interpretation.

There is another no direct identification case of Ca-rich SN Ib 2019ehk (Jacobson-Galán et al. 2020), which is not presented in Figure 8 and Table 3. Its absolute detection limit from the pre-explosion image is -2.4 mag in $F555W$ filter ($HST/WFPC2$) under the host galaxy distance assumption of $d = 16.2$ Mpc. The progenitor of SN 2019ehk is not detected although the detection limit is far higher than the HE model predictions ($M_{F555W} = -4 \dots -6$). This result is consistent with the scenario that Ca-rich SNe Ib would have a white dwarf origin instead of massive stars (e.g., Perets et al. 2011; Kasliwal et al. 2012).

We obtain the upper limit of the progenitor mass-loss rate (\dot{M}_{max}) by comparing various mass-loss rate models with detection limits of pre-explosion images, and summarize the results in Table 3. These upper limits are obtained by comparing the detection limits with HE and relatively massive ($M \gtrsim 5 M_{\odot}$) CO model predictions. All of our relatively low-mass CO2.16/CO3.83 models are below the detection limits and cannot provide a upper limit for our considered parameter space. This result implies that if the progenitors of observed SNe Ib/Ic had a mass-loss rate comparable to \dot{M}_{fid} , non-detection would be a natural consequence for most cases, and that deeper observations with an optical absolute magnitude larger than about $-4 \dots -5$ are needed to directly observe the progenitors and to make a better constraint on their properties. The point source magnitude limit with an optical wide band filter in $HST/WFC3$ for 1 hour observation is $\sim 27.1 - 27.9$ mag (at a signal-to-noise ratio of 10). This means that a progenitor with the absolute

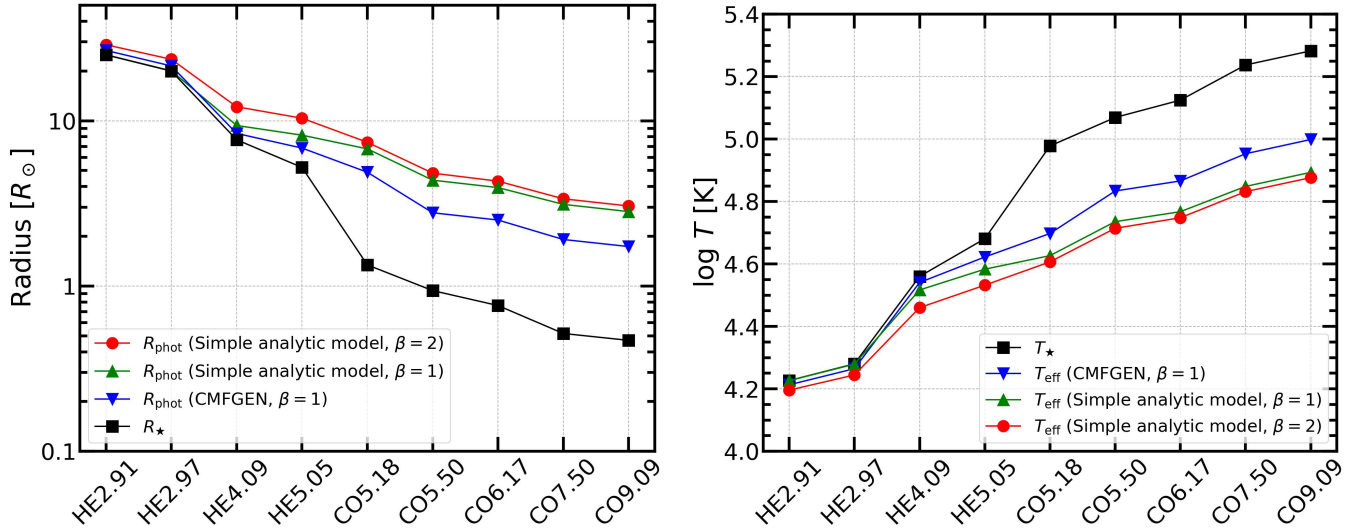


Figure 7. Comparison of photospheric parameters of the SN Ib/Ic progenitor models calculated by the simple analytic model and the non-LTE CMFGEN code. The green triangle ($\beta = 1$) and red circle ($\beta = 2$) give the photospheric radius and the effective temperature calculated by the simple analytic model. The CMFGEN results are plotted with blue inverted triangles. The radius and temperature at the hydrostatic surface are denoted by black squares for comparison.

Table 3. Upper limits of the mass-loss rate of the non-detected SN Ib/Ic progenitors in previous searches and constraints on the possible companion stellar mass

Type	Name	\dot{M}_{\max}^a	$M_{\text{comp,max}}^b$	$M_{\text{comp,max}}^b$
			(ZAMS)	(Evolved)
SN Ib	SN 2001B			
	SN 2011am			$< 85 M_{\odot}$
	SN 2012au			$< 85 M_{\odot}$
SN Ib/Ic	SN 2004gt		$< 120 M_{\odot}$	$< 40 M_{\odot}$
	SN 2005V			
	SN 2010br	$< \dot{M}_{\text{fid}} \times 5.0$	$< 60 M_{\odot}$	$< 20 M_{\odot}$
SN Ic	SN 2000ew			$< 60 M_{\odot}$
	SN 2002ap	$< \dot{M}_{\text{fid}} \times 1.0$	$< 32 M_{\odot}$	$< 15 M_{\odot}$
	SN 2003jg	$< \dot{M}_{\text{fid}} \times 10.0$	$< 120 M_{\odot}$	$< 40 M_{\odot}$
	SN 2004gn	$< \dot{M}_{\text{fid}} \times 5.0$	$< 80 M_{\odot}$	$< 32 M_{\odot}$
	SN 2007gr			$< 40 M_{\odot}$
	SN 2011hp	$< \dot{M}_{\text{fid}} \times 10.0$	$< 120 M_{\odot}$	$< 40 M_{\odot}$
	SN 2020oi	$< \dot{M}_{\text{fid}} \times 2.0$	$< 32 M_{\odot}$	$< 15 M_{\odot}$

NOTE—Detection limits are from the *HST*/WFPC2 images except SN 2002ap and SN 2020oi from Johnson-B and *HST*/WFC3 image, respectively.

^aUpper limits of the mass-loss rates are obtained by comparing with HE and relatively massive ($M \gtrsim 5 M_{\odot}$) CO model predictions. Blank if a detection limit is brighter than the progenitor model with $\dot{M}_{\text{fid}} \times 10.0$.

^bBlank if a detection limit is brighter than the ZAMS or evolved $120 M_{\odot}$ O type star.

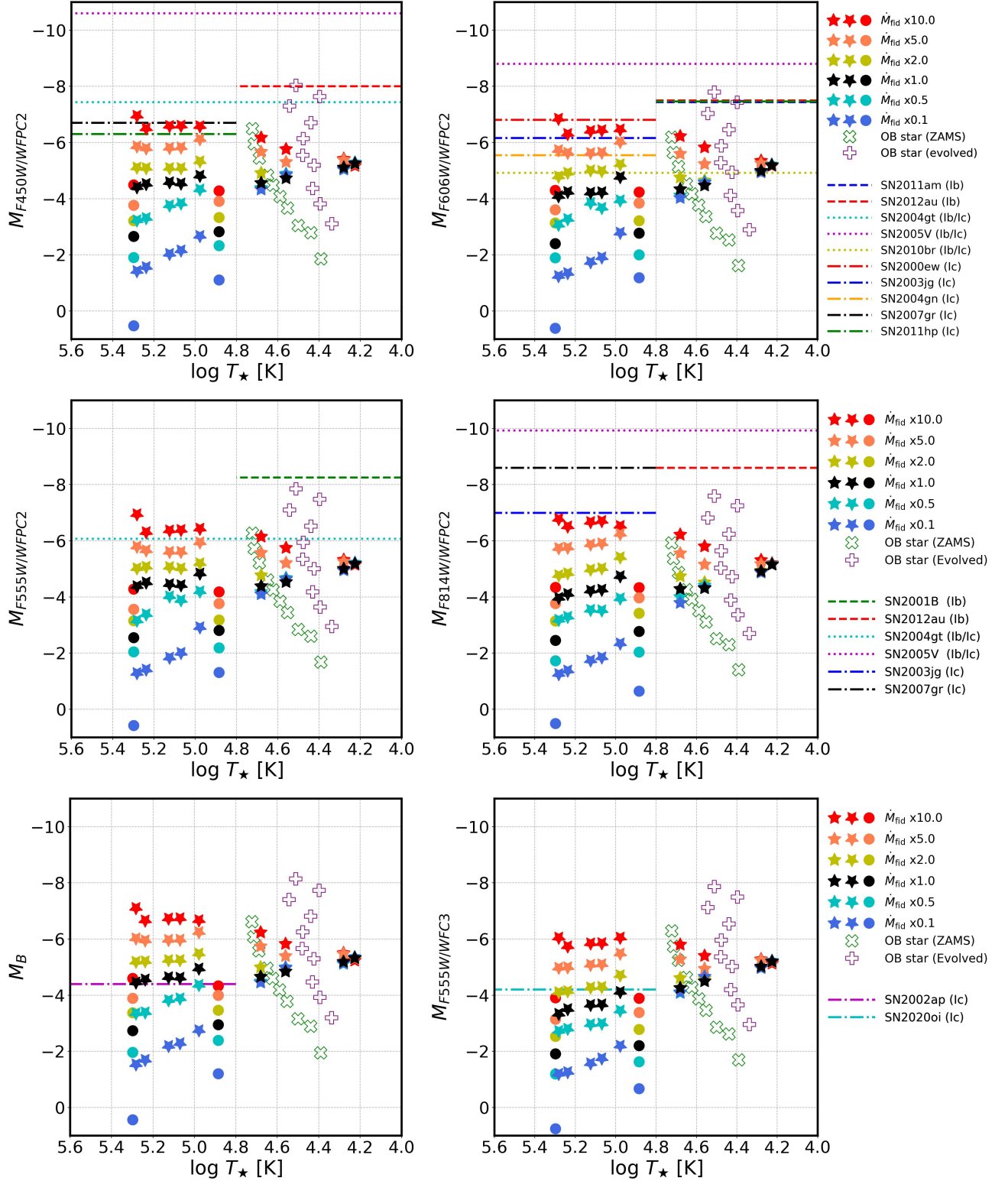


Figure 8. Optical magnitude of progenitor models and the detection limits from the pre-explosion images of SNe Ib/Ic. Each panel shows the absolute magnitude of progenitor models in different filters : $F450W$, $F555W$, $F606W$ and $F814W$ in $HST/WFPC2$, Johnson-B and $F555W$ in $HST/WFC3$. The detection limits from the pre-explosion images of SNe Ib, Ic and Ib/Ic are plotted in dashed, dash-dotted and dotted lines, respectively (Eldridge et al. 2013; Gagliano et al. 2021). Optical magnitude of O/B type stars with 9, 12, 15, 20, 25, 32, 40, 60, 85 and $120 M_{\odot}$ are plotted together in green (ZAMS) and purple (evolved) marker for the comparison (Fierro et al. 2015). Each color gives the adopted mass-loss rate as indicated by the labels.

optical magnitude of -4 mag would be detected only if it were in a galaxy closer than $\sim 16 - 24$ Mpc. The limiting distance can be decreased to $\sim 10 - 15$ Mpc for 10 min observation. The host galaxy extinction should be additionally considered for a more precise distance limit.

Many SN Ib/Ic progenitors would be produced in binary systems and the contribution of the companion star to the optical brightness would also be significant. We take CMFGEN model spectra of O/B type stars at zero-age main sequence (ZAMS) and an evolved phase on the main sequence having the initial mass range of $9 - 120 M_{\odot}$ from Fierro et al. (2015), and present their optical magnitudes in Figure 8. Our fiducial progenitor models have optical magnitudes comparable to those of $15 - 25 M_{\odot}$ evolved O stars or $25 - 60 M_{\odot}$ O stars at ZAMS. For each progenitor, we get the upper limit of the possible companion star mass ($M_{\text{comp,max}}$) by comparing the detection limit with the O/B star magnitudes, ignoring the contribution from the SN progenitor. The result is summarized in Table 3. Even for the deepest detection limit cases, we can only exclude a companion star more massive than $15 M_{\odot}$.

Zapartas et al. (2017) predict the possible companions of stripped-envelope SNe at the explosion time using the population synthesis simulation. The result of the study shows that only ~ 20 % of stripped-envelope SNe progenitors would have massive a companion with $> 20 M_{\odot}$. This result also implies that most SN Ib/Ic progenitors would not have massive companion star that is bright enough to exceed the previous detection limits.

4.2. Comparison with the progenitor candidate of SN Ib iPTF13bvn

The progenitor candidate of Type Ib SN iPTF13bvn in NGC 5806 is reported by Cao et al. (2013) and later convincingly identified as the progenitor by a follow-up observation by Eldridge & Maund (2016); Folatelli et al. (2016). Cao et al. (2013) measure the Milky Way and host galaxy reddening as $E(B - V)_{MW} = 0.0278$ and $E(B - V)_{\text{host}} = 0.0437$, respectively, from the Na I D lines and use the adopted distance modulus of $\mu = 31.76 \pm 0.36$ (22.5 ± 2.4 Mpc) (Tully et al. 2009). Their photometry of the progenitor candidate gives the values of $m_{F435W} = 26.50 \pm 0.15$, $m_{F555W} = 26.40 \pm 0.15$ and $m_{F814W} = 26.10 \pm 0.20$ mag in the *HST* Advanced Camera for Surveys (ACS) filter system.

On the other hand, Bersten et al. (2014) suggest higher extinction values of $E(B - V)_{MW} = 0.0447$ and $E(B - V)_{\text{host}} = 0.17$ using the SN light curve and Na I lines. Moreover, Eldridge et al. (2015) give brighter photometry values of $m_{F435W} = 25.80 \pm 0.12$,

$m_{F555W} = 25.80 \pm 0.11$ and $m_{F814W} = 25.88 \pm 0.24$ mag for the same progenitor candidate. In this study, we present the results of every combination of different extinctions and photometry values.

In Figure 9, we show our HE progenitor models and the iPTF13bvn progenitor candidate in the color-magnitude diagram and the color-color diagram. We present four observational results together. For the photometry result of Cao et al. (2013), the magnitude and the color of iPTF13bvn progenitor can be explained by the relatively low-mass fiducial models HE2.91 and HE2.97 or by most HE models with $\dot{M}_{\text{fid}} \times 5 \dots 10$. For the photometry result of Eldridge et al. (2015), however, the progenitor candidate of the iPTF13bvn is brighter than most of our considered HE models, being about 1 mag brighter than the fiducial models in the optical. Only the HE4.09 and HE5.05 models with $\dot{M}_{\text{fid}} \times 10.0$ can explain the optical brightness. The inferred ejecta mass ($\sim 2.0 - 2.3 M_{\odot}$) and helium core mass ($\sim 3.4 - 3.5 M_{\odot}$) of iPTF13bvn (Bersten et al. 2014; Fremling et al. 2014) are in range of our HE models.

To consider the possible contribution from a companion star of the progenitor, we also calculate the composite magnitudes from the spectral models of both the HE progenitors and the evolved main sequence stars of $M_{\text{init}} = 9$ and $25 M_{\odot}$ from Fierro et al. (2015). As seen in Figure 10, the optical properties of the iPTF13bvn progenitor candidate are consistent with the models with a $9 M_{\odot}$ or $25 M_{\odot}$ companion star for photometry result of Cao et al. (2013) and Eldridge et al. (2015), respectively. A $9 M_{\odot}$ companion would be a reasonable solution within the standard binary scenario of SN Ib progenitors (e.g., Bersten et al. 2014; Yoon 2017) and agrees well with other previous studies on iPTF13bvn (e.g., Fremling et al. 2014; Srivastav et al. 2014; Kun-carayakti et al. 2015; Fremling et al. 2016; Folatelli et al. 2016; Eldridge & Maund 2016). A companion star as massive as $25 M_{\odot}$ is somewhat hard to explain. Given that the inferred ejecta mass of iPTF13bvn is only about $2.0 M_{\odot}$, such a massive companion in a binary system could be produced only with conservative mass transfer and an unusually high mass-loss rate from the naked primary star during the post-mass transfer phase (Wellstein & Langer 1999). On the other hand, Groh et al. (2013a) suggest a single WR star progenitor (initial mass $M_{\text{init}} = 31 - 35 M_{\odot}$) by comparing of the Geneva single star evolution model with the observation., but the predicted pre-explosion mass of $M \simeq 10.9 M_{\odot}$ is incompatible with the inferred ejecta mass of iPTF13bvn.

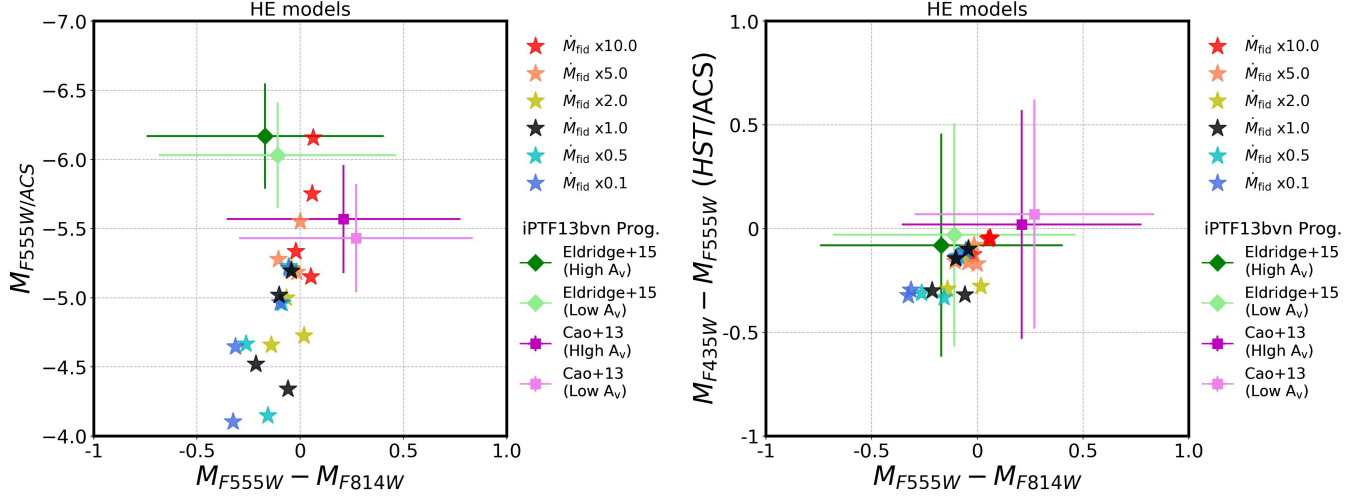


Figure 9. Color-magnitude diagram (left) and color-color diagram (right) of the HE models. The absolute optical magnitudes and colors of the iPTF13bvn progenitor candidate for two different extinction and photometry values are presented together. Magenta and green markers denote the values calculated with the photometry results of Cao et al. (2013) and Eldridge et al. (2015), respectively. The values with high and low extinction assumptions are plotted in dark and light colors, respectively.

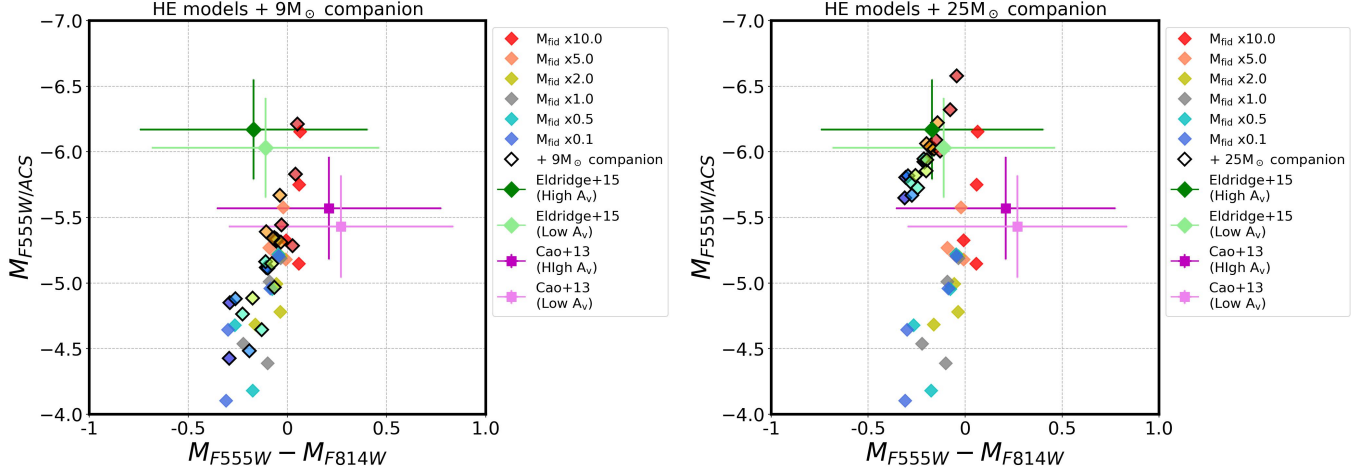


Figure 10. Color-magnitude diagrams of the HE progenitor models. The left and right panel give the composite results with a $9M_{\odot}$ and a $25M_{\odot}$ companion star, respectively. The diamond markers without a black border denote the progenitor models without a companion star, and the filled diamonds with black border denote the composite models with a companion star. Each color of the markers gives the adopted mass-loss rate as indicated by the labels. The values of the iPTF13bvn progenitor candidate are plotted together as in Figure 9.

4.3. Comparison with the progenitor candidate of SN Ib 2019yvr

Kilpatrick et al. (2021) report the SN Ib progenitor candidate of SN 2019yvr, which is found ~ 980 to 870 days (~ 2.6 years) before the explosion in a *HST*/WFC3 observation. The average photometry across all epochs in four bands gives the results of $m_{F438W} = 26.138 \pm 0.162$, $m_{F555W} = 25.351 \pm 0.032$, $m_{F625W} = 24.897 \pm 0.022$ and $m_{F814W} = 24.253 \pm 0.032$ mag. The color corrected only with the Milky Way extinction $E(B-V)_{MW} = 0.02$

is $m_{F555W} - m_{F814W} = 1.065 \pm 0.045$ mag, which corresponds to the temperature of $T_{\text{eff}} = 3340$ K. Without a fairly high host galaxy extinction, the color is too red to be explained by our HE progenitor models (see the values in Figure 9).

Kilpatrick et al. (2021) obtained the high host galaxy extinction value of $A_V = 2.4^{+0.7}_{-1.1}$ and $R_V = 4.7^{+1.3}_{-3.0}$ from Na I D spectra and color curves of SN 2019yvr. They infer the physical parameters of the progenitor candidate by fitting with the single star SEDs from Pickles & Depagne (2010). The best-fitting values are $T_{\text{eff}} = 6800$

K, $\log(L/L_\odot) = 5.3 \pm 0.2$ and $R_{\text{phot}} = 320 R_\odot$ from F2I star model, and they argue that this large radius of the photosphere might be explained by a very high mass-loss rate of $\sim 10^{-4} M_\odot \text{ yr}^{-1}$. To check this possibility, we construct spectra of our most massive HE model (HE5.05) with mass-loss rates up to $100 \times \dot{M}_{\text{fid}}$ and present the results in Table 4 and Figure 11. We find that the models with very high mass-loss rates (i.e., $\dot{M} = 50 \cdots 100 \times \dot{M}_{\text{fid}}$) can explain the optical color and magnitudes of the progenitor candidate. The SN 2019yvr progenitor candidate is observed during 980 to 870 days before the explosion. Although stellar evolution models predict that the surface properties of SN Ib progenitors would not undergo a rapid change during the pre-explosion phase (Yoon et al. 2017), the inferred high mass-loss rate implies that the progenitor underwent mass eruption shortly before the explosion, for which energy injection from the inner convective layers via wave heating during core neon/oxygen burning might be a possible explanation (Fuller & Ro 2018; Leung et al. 2021). Note also that evidence for pre-SN mass eruption is found in the early-time light curves of some stripped-envelope supernovae (e.g., Jin et al. 2021). However, the observational signature of late time interaction of SN 2019yvr (Kilpatrick et al. 2021) is not likely to be related to this mass eruption because the matter emitted during the last several years would be confined to a small radius ($\lesssim 10^{15}$ cm) from the progenitor at the time of explosion and would affect only the early-time SN light curve (see Jin et al. 2021).

Here we obtain the extinction corrected absolute magnitude of the progenitor candidate with the host galaxy extinction ($A_V = 2.4$ and $R_V = 4.7$) and distance modulus ($m - M = 30.8 \pm 0.2$ mag) adopted from Kilpatrick et al. (2021). The corrected values are $M_{F438W} = -7.7 \pm 0.3$, $M_{F555W} = -7.8 \pm 0.2$, $M_{F625W} = -8.0 \pm 0.2$ and $M_{F814W} = -8.0 \pm 0.2$ mag for each *HST*/WFC3 filter. The adopted host galaxy extinction values, however, are obtained from the observation after the SN explosion, so we have to consider the possibility of additional extinction sources (e.g. dusty circumstellar matter) before the explosion. If there were additional extinction sources, the corrected magnitudes and the color would move to the brighter and bluer direction away from the model predictions.

4.4. Comparison with the progenitor candidate of SN Ic 2017ein

There is a progenitor candidate for SN Ic 2017ein. Kilpatrick et al. (2018) suggest the Milky Way extinction of

$A_V = 0.058$ ($R_V = 3.1$) and the host galaxy extinction of $A_V = 1.2$ ($R_V = 2.6$). With the distance modulus $\mu = 31.17 \pm 0.10$ for NGC 3938 (Tully et al. 2009), the extinction corrected magnitudes are obtained as $M_{F555W} = -7.5 \pm 0.2$ mag and $M_{F814W} = -6.7 \pm 0.2$ mag for each *HST*/WFPC2 filter. Van Dyk et al. (2018) independently analyze the *HST* photometric data before the explosion, and obtain a similar result with various extinction assumptions, as shown in Figure 12. In the figure, this candidate is compared with our CO progenitor models, the progenitor candidate is much more luminous than our fiducial models in the optical (by about 2 mag) and only a very high mass-loss rate of $\dot{M}_{\text{fid}} \times 10.0$ can result in a barely comparable magnitude in the *F814W* filter. The observed color ($M_{F555W} - M_{F814W}$) is very blue compared to our progenitor models. No model within our parameter space satisfies both the observed magnitude and color of this candidate.

We also consider O/B type evolved main-sequence companion stars of 9, 25, and 120 M_\odot whose spectra are taken from Fierro et al. (2015) and the composite magnitudes and colors with the CO progenitor models are plotted in Figure 12. Since our most massive CO progenitor model (CO9.09) is evolved from a 25 M_\odot He star, which corresponds to $M_{\text{init}} \approx 65 M_\odot$, a companion star with 120 M_\odot is not realistic. The upper right panel of Figure 12 shows, however, that even this unrealistically massive companion cannot explain the blue color of the progenitor candidate.

On the other hand, all of the composite models with 9 and 25 M_\odot companion stars are fainter and redder than the candidate (the lower panels of Figure 12). Under the assumption that the values inferred from the observation are reliable, we conclude that the reported candidate of SN 2017ein is too blue and too bright in the optical to be explained by a typical SN Ic progenitor.

Kilpatrick et al. (2018) suggest a 55 M_\odot single star or a 80 + 48 M_\odot binary at ZAMS as the progenitor. Van Dyk et al. (2018) suggest a $\sim 47 - 48 M_\odot$ single star or a $\sim 60 - 80 M_\odot$ in binary at ZAMS. Our SN Ic progenitor models cover this initial mass range since our most massive model (CO9.09) corresponds to a 60 - 70 M_\odot star at ZAMS. Kilpatrick et al. (2018) obtain a host galaxy extinction value of $A_V = 1.2 - 1.9$ using Na I lines. The extinction corrected color and magnitude of the SN 2017ein progenitor candidate are calculated using the lowest value of $A_V = 1.2$, but it is already too bright and blue. Moreover, there can be additional extinction sources before the explosion, which can make it move to brighter and bluer region. Van Dyk et al. (2018) presents a similar result in spite of the various

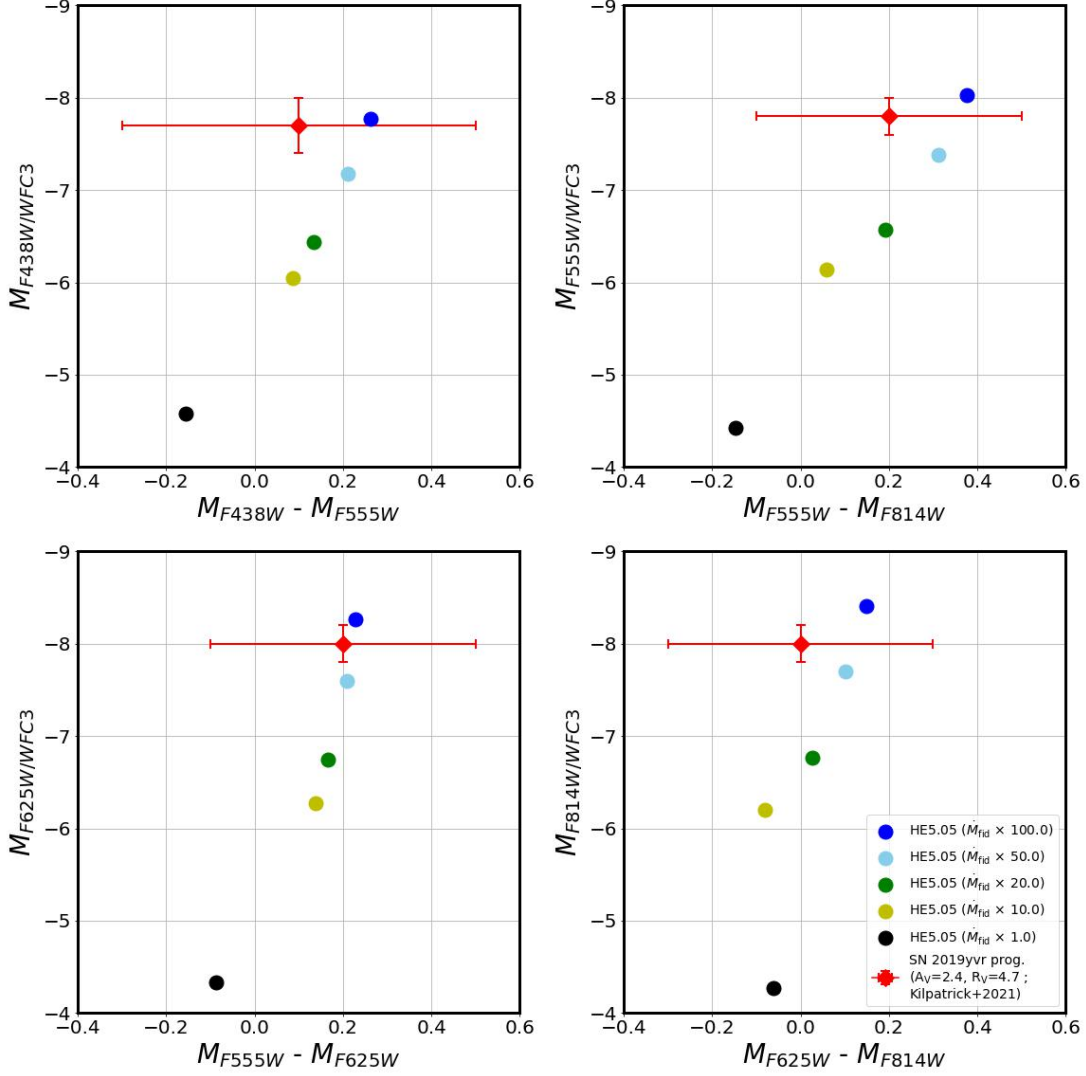


Figure 11. Color-magnitude diagrams of SN 2019yvr progenitor candidate comparing with SN Ib progenitor models. SN 2019yvr progenitor candidate and HE5.05 models are plotted in diamond and circles, respectively. The color denotes the adopted mass-loss rate of HE5.05 models as indicated by the labels. Color and absolute magnitude of SN 2019yvr progenitor are corrected under the assumption of $A_V = 2.4$ and $R_V = 4.7$.

Table 4. Physical parameters of the progenitor candidate of SN 2019yvr and SN Ib progenitor models

	SN 2019yvr	HE5.05	HE5.05	HE5.05	HE5.05	HE5.05
	(Kilpatrick et al. 2021)	(\dot{M}_{fid})	($\dot{M}_{\text{fid}} \times 10$)	($\dot{M}_{\text{fid}} \times 20$)	($\dot{M}_{\text{fid}} \times 50$)	($\dot{M}_{\text{fid}} \times 100$)
$\log L/L_\odot$	5.3	5.1	5.1	5.1	5.1	5.1
\dot{M} [$M_\odot \text{ yr}^{-1}$]	$>1.4\text{e-}04$	$8.13\text{e-}06$	$8.13\text{e-}05$	$1.63\text{e-}04$	$4.06\text{e-}04$	$8.13\text{e-}04$
T_{eff} [K]	6800	41910	18660	14260	10230	7852
R_{phot} [R_\odot]	320	6.834	34.49	59.03	114.7	194.7

NOTE—First column shows the physical parameters of the best-fit single star progenitor model (F2I model from Pickles & Depagne (2010)) for SN 2019yvr from Kilpatrick et al. (2021). The other columns show the physical parameters of HE5.05 model with various mass-loss rates. HE5.05 model is evolved from a $8 M_\odot$ helium star, which corresponds to a $\sim 25 M_\odot$ star at ZAMS.

extinction assumptions. To confirm if the observed can-

didate was the real progenitor or not, we need additional observation to check the disappearance of the candidate.

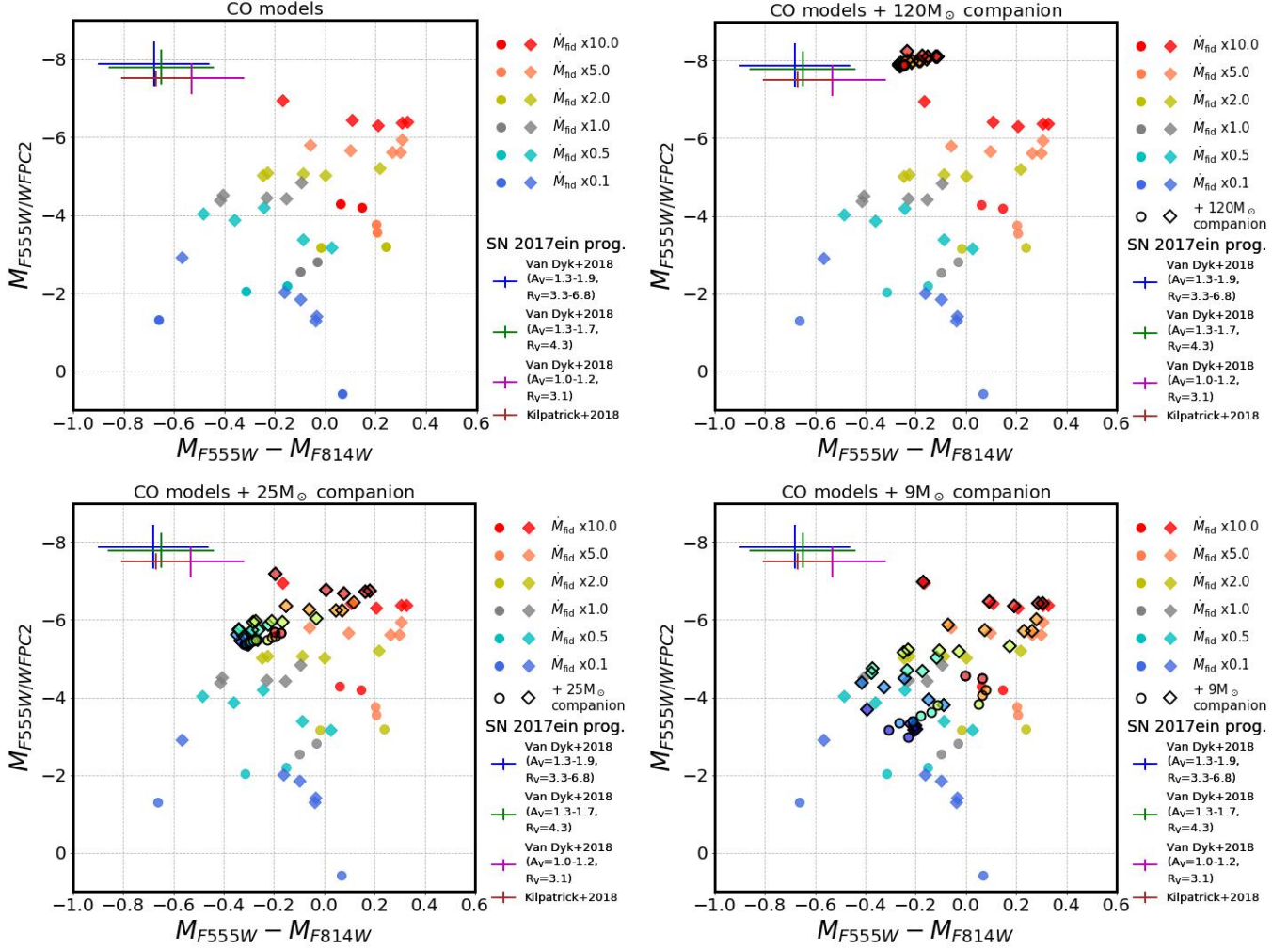


Figure 12. Color-magnitude diagrams of CO progenitor models. The upper left panel gives the results without considering a companion star. The upper right, lower left, and lower right panels present the composite results with a 120, 25, and 9 M_{\odot} companion star, respectively. The diamond and circle marker with/without a black border denotes the progenitor models with/without a companion star. The reported magnitude and color of SN 2017ein progenitor candidate are plotted together for comparison. Each color gives the adopted mass-loss rate as indicated by the labels.

5. CONCLUSIONS

We present stellar atmosphere models of SN Ib/Ic progenitors having different chemical compositions for the pre-SN mass range of 2.16 – 9.09 M_{\odot} , which are calculated by the non-LTE radiative transfer code CMFGEN. We investigate the effects of various wind parameters on the resulting spectra and optical properties and discuss implications of our results for direct identification of SN Ib/Ic progenitors.

Our results indicate that optical properties of SN Ib/Ic progenitors can be greatly affected by the presence of optically thick wind, and inferring SN Ib/Ic progenitor masses and bolometric luminosities from optical brightness and colors observed in pre-SN images could be misleading. More specifically, we draw the following conclusions from our discussions.

1. Presence of sufficiently high density wind material around a SN Ib/Ic progenitor can make the photosphere significantly lifted-up from the hydrostatic stellar surface. Strong emission lines and free-free emission from the optical thick wind can also critically affect optical magnitudes. These effects would generally make SN Ib/Ic progenitors brighter in the optical compared to the corresponding case without winds, in particular for helium-deficient compact SN Ic progenitors. Our models predict that SN Ic progenitors would be brighter by more than 3 mag in the optical than the case without the wind effects for the fiducial WR mass-loss rate. On the other hand, optical properties of SN Ib progenitors having an extended helium-rich envelope are not greatly affected by

- the effects of winds for the fiducial WR mass-loss rate. The optical brightness becomes higher for a higher mass-loss rate (or a lower wind terminal velocity), and this tendency is found more clearly for a more compact progenitor (Sections 3.1 and 3.2).
2. The wind effects also greatly affect the color of SN Ib/Ic progenitors. In general, the color becomes redder for a higher mass-loss rate (or a lower wind terminal velocity) because of the lifting-up of the photosphere and the continuum excess due to free-free emission in a relatively long wavelength range. However, the optical colors are not well correlated with the effective temperature, nor with the hydrostatic surface temperature. This is because strong emission lines found in specific filters and the free-free emission make the color-temperature relations highly non-monotonic (Sections 3.1 and 3.2).
 3. For a typical mass-loss rate of WR stars, the optical brightness of most SN Ib/Ic progenitors would not be high enough to be detected within the detection limits of previous searches in pre-SN images. Also, these detection limits were not deep enough to observe companion stars of $M_{\text{comp}} < 15 M_{\odot}$, which would be the typical case for SN Ib/Ic progenitors. A deep search with an optical absolute magnitude larger than ~ -4 would be needed for identification of most of ordinary SN Ib/Ic progenitors. The distance limit for a direct progenitor detection is $\sim 10 - 15$ Mpc and $\sim 16 - 24$ Mpc for 10 min and 1 hour observation, respectively, for an optical wide band filter of *HST*/WFC3. (Section 4.1).
 4. The optical brightness and color of the observed SN Ib iPTF13bvn progenitor can be explained by our models within the considered parameter space. The photometry result of Cao et al. (2013) is consistent with the relatively low-mass fiducial HE models (HE2.91 and HE2.97), HE4.09/HE5.05 models with a relatively high mass-loss rate ($\dot{M}_{\text{fid}} \times 5 \cdots 10$) or existence of a $\sim 9 M_{\odot}$ companion star. For the photometry result of Eldridge et al. (2015), the optical brightness and color of the progenitor can be explained by HE4.09/HE5.05 models with a very high mass-loss rate ($\dot{M}_{\text{fid}} \times 10$) or with the existence of $\sim 25 M_{\odot}$ companion star (Section 4.2).
 5. The SN Ib 2019yvr progenitor candidate is very bright and red in the optical compared to our fiducial HE models. Its optical brightness and color can be explained by the HE5.05 model with an unusually high mass-loss rate of $\dot{M}_{\text{fid}} \times 50 \cdots 100$. This implies the SN 2019yvr progenitor experienced mass-loss enhancement shortly before the SN explosion (Section 4.3).
 6. The SN Ic 2017ein progenitor candidate is too blue and bright to be explained with any of our models whether we consider a companion star or not. Any known massive stars could not explain both the optical brightness and the blue color of this progenitor candidate (Section 4.4).
- 1 This work has been supported by the National Research Foundation of Korea (NRF) grant (NRF-2019R1A2C2010885). We are grateful to John Hillier for making the CMFGEN code publicly available and for the helps he gave us at the beginning of this project.

REFERENCES

- Bersten, M. C., Benvenuto, O. G., Folatelli, G., et al. 2014, *AJ*, 148, 68, doi: [10.1088/0004-6256/148/4/68](https://doi.org/10.1088/0004-6256/148/4/68)
- Cano, Z. 2013, *MNRAS*, 434, 1098, doi: [10.1093/mnras/stt1048](https://doi.org/10.1093/mnras/stt1048)
- Cao, Y., Kasliwal, M. M., Arcavi, I., et al. 2013, *ApJL*, 775, L7, doi: [10.1088/2041-8205/775/1/L7](https://doi.org/10.1088/2041-8205/775/1/L7)
- Cidale, L. S., Arias, M. L., Torres, A. F., et al. 2007, *A&A*, 468, 263, doi: [10.1051/0004-6361:20066454](https://doi.org/10.1051/0004-6361:20066454)
- De Loore, C., Hellings, P., & Lamers, H. J. G. 1982, in *Wolf-Rayet Stars: Observations, Physics, Evolution*, ed. C. W. H. De Loore & A. J. Willis, Vol. 99, 53–56
- Dessart, L., Yoon, S.-C., Aguilera-Dena, D. R., & Langer, N. 2020, *A&A*, 642, A106, doi: [10.1051/0004-6361/202038763](https://doi.org/10.1051/0004-6361/202038763)
- Drew, J. E., Barlow, M. J., Unruh, Y. C., et al. 2004, *MNRAS*, 351, 206, doi: [10.1111/j.1365-2966.2004.07771.x](https://doi.org/10.1111/j.1365-2966.2004.07771.x)
- Drout, M. R., Soderberg, A. M., Gal-Yam, A., et al. 2011, *ApJ*, 741, 97, doi: [10.1088/0004-637X/741/2/97](https://doi.org/10.1088/0004-637X/741/2/97)
- Ekström, S., Georgy, C., Eggenberger, P., et al. 2012, *A&A*, 537, A146, doi: [10.1051/0004-6361/201117751](https://doi.org/10.1051/0004-6361/201117751)
- Eldridge, J. J., Fraser, M., Maund, J. R., & Smartt, S. J. 2015, *MNRAS*, 446, 2689, doi: [10.1093/mnras/stu2197](https://doi.org/10.1093/mnras/stu2197)

- Eldridge, J. J., Fraser, M., Smartt, S. J., Maund, J. R., & Crockett, R. M. 2013, *MNRAS*, 436, 774, doi: [10.1093/mnras/stt1612](https://doi.org/10.1093/mnras/stt1612)
- Eldridge, J. J., Izzard, R. G., & Tout, C. A. 2008, *MNRAS*, 384, 1109, doi: [10.1111/j.1365-2966.2007.12738.x](https://doi.org/10.1111/j.1365-2966.2007.12738.x)
- Eldridge, J. J., & Maund, J. R. 2016, *MNRAS*, 461, L117, doi: [10.1093/mnrasl/slw099](https://doi.org/10.1093/mnrasl/slw099)
- Eldridge, J. J., & Vink, J. S. 2006, *A&A*, 452, 295, doi: [10.1051/0004-6361:20065001](https://doi.org/10.1051/0004-6361:20065001)
- Fierro, C. R., Borissova, J., Zsargó, J., et al. 2015, *PASP*, 127, 428, doi: [10.1086/681703](https://doi.org/10.1086/681703)
- Folatelli, G., Van Dyk, S. D., Kuncarayakti, H., et al. 2016, *ApJL*, 825, L22, doi: [10.3847/2041-8205/825/2/L22](https://doi.org/10.3847/2041-8205/825/2/L22)
- Fremling, C., Sollerman, J., Taddia, F., et al. 2014, *A&A*, 565, A114, doi: [10.1051/0004-6361/201423884](https://doi.org/10.1051/0004-6361/201423884)
- . 2016, *A&A*, 593, A68, doi: [10.1051/0004-6361/201628275](https://doi.org/10.1051/0004-6361/201628275)
- Fuller, J., & Ro, S. 2018, *MNRAS*, 476, 1853, doi: [10.1093/mnras/sty369](https://doi.org/10.1093/mnras/sty369)
- Gagliano, A., Izzo, L., Kilpatrick, C. D., et al. 2021, arXiv e-prints, arXiv:2105.09963, <https://arxiv.org/abs/2105.09963>
- Georgy, C., Ekström, S., Meynet, G., et al. 2012, *A&A*, 542, A29, doi: [10.1051/0004-6361/201118340](https://doi.org/10.1051/0004-6361/201118340)
- Gräfener, G., & Hamann, W. R. 2008, *A&A*, 482, 945, doi: [10.1051/0004-6361:20066176](https://doi.org/10.1051/0004-6361:20066176)
- Groh, J. H., Georgy, C., & Ekström, S. 2013a, *A&A*, 558, L1, doi: [10.1051/0004-6361/201322369](https://doi.org/10.1051/0004-6361/201322369)
- Groh, J. H., Meynet, G., Georgy, C., & Ekström, S. 2013b, *A&A*, 558, A131, doi: [10.1051/0004-6361/201321906](https://doi.org/10.1051/0004-6361/201321906)
- Hachinger, S., Mazzali, P. A., Taubenberger, S., et al. 2012, *MNRAS*, 422, 70, doi: [10.1111/j.1365-2966.2012.20464.x](https://doi.org/10.1111/j.1365-2966.2012.20464.x)
- Hainich, R., Rühling, U., Todt, H., et al. 2014, *A&A*, 565, A27, doi: [10.1051/0004-6361/201322696](https://doi.org/10.1051/0004-6361/201322696)
- Hamann, W. R., Gräfener, G., & Liermann, A. 2006, *A&A*, 457, 1015, doi: [10.1051/0004-6361:20065052](https://doi.org/10.1051/0004-6361:20065052)
- Hamann, W. R., & Koesterke, L. 1998, *A&A*, 335, 1003
- Hamann, W. R., Gräfener, G., Liermann, A., et al. 2019, *A&A*, 625, A57, doi: [10.1051/0004-6361/201834850](https://doi.org/10.1051/0004-6361/201834850)
- Hillier, D. J. 1990, *A&A*, 231, 116
- Hillier, D. J., Lanz, T., Heap, S. R., et al. 2003, *ApJ*, 588, 1039, doi: [10.1086/374329](https://doi.org/10.1086/374329)
- Hillier, D. J., & Miller, D. L. 1998, *ApJ*, 496, 407, doi: [10.1086/305350](https://doi.org/10.1086/305350)
- Hunger, K., & Klinglesmith, D. 1969, *ApJ*, 157, 721, doi: [10.1086/150109](https://doi.org/10.1086/150109)
- Jacobson-Galán, W. V., Margutti, R., Kilpatrick, C. D., et al. 2020, *ApJ*, 898, 166, doi: [10.3847/1538-4357/ab9e66](https://doi.org/10.3847/1538-4357/ab9e66)
- Jin, H., Yoon, S.-C., & Blinnikov, S. 2021, *ApJ*, 910, 68, doi: [10.3847/1538-4357/abe0b1](https://doi.org/10.3847/1538-4357/abe0b1)
- Kasliwal, M. M., Kulkarni, S. R., Gal-Yam, A., et al. 2012, *ApJ*, 755, 161, doi: [10.1088/0004-637X/755/2/161](https://doi.org/10.1088/0004-637X/755/2/161)
- Kilpatrick, C. D., Takaro, T., Foley, R. J., et al. 2018, *MNRAS*, 480, 2072, doi: [10.1093/mnras/sty2022](https://doi.org/10.1093/mnras/sty2022)
- Kilpatrick, C. D., Drout, M. R., Auchettl, K., et al. 2021, *MNRAS*, 504, 2073, doi: [10.1093/mnras/stab838](https://doi.org/10.1093/mnras/stab838)
- Kim, H.-J., Yoon, S.-C., & Koo, B.-C. 2015, *ApJ*, 809, 131, doi: [10.1088/0004-637X/809/2/131](https://doi.org/10.1088/0004-637X/809/2/131)
- Kuncarayakti, H., Maeda, K., Bersten, M. C., et al. 2015, *A&A*, 579, A95, doi: [10.1051/0004-6361/201425604](https://doi.org/10.1051/0004-6361/201425604)
- Lamers, H. J. G. L. M., & Cassinelli, J. P. 1999, *Introduction to Stellar Winds*
- Langer, N. 1989, *A&A*, 210, 93
- Leung, S.-C., Wu, S., & Fuller, J. 2021, arXiv e-prints, arXiv:2110.01565, <https://arxiv.org/abs/2110.01565>
- Lyman, J. D., Bersier, D., & James, P. A. 2014, *MNRAS*, 437, 3848, doi: [10.1093/mnras/stt2187](https://doi.org/10.1093/mnras/stt2187)
- Mazzali, P. A., Kawabata, K. S., Maeda, K., et al. 2007, *ApJ*, 670, 592, doi: [10.1086/521873](https://doi.org/10.1086/521873)
- Meynet, G., & Maeder, A. 2005, *A&A*, 429, 581, doi: [10.1051/0004-6361:20047106](https://doi.org/10.1051/0004-6361:20047106)
- Nugis, T., & Lamers, H. J. G. L. M. 2000, *A&A*, 360, 227
- Paxton, B., Bildsten, L., Dotter, A., et al. 2011, *ApJS*, 192, 3, doi: [10.1088/0067-0049/192/1/3](https://doi.org/10.1088/0067-0049/192/1/3)
- Paxton, B., Cantiello, M., Arras, P., et al. 2013, *ApJS*, 208, 4, doi: [10.1088/0067-0049/208/1/4](https://doi.org/10.1088/0067-0049/208/1/4)
- Paxton, B., Marchant, P., Schwab, J., et al. 2015, *ApJS*, 220, 15, doi: [10.1088/0067-0049/220/1/15](https://doi.org/10.1088/0067-0049/220/1/15)
- Paxton, B., Schwab, J., Bauer, E. B., et al. 2018, *ApJS*, 234, 34, doi: [10.3847/1538-4365/aaa5a8](https://doi.org/10.3847/1538-4365/aaa5a8)
- Paxton, B., Smolec, R., Schwab, J., et al. 2019, *ApJS*, 243, 10, doi: [10.3847/1538-4365/ab2241](https://doi.org/10.3847/1538-4365/ab2241)
- Perets, H. B., Badenes, C., Arcavi, I., Simon, J. D., & Gal-yam, A. 2011, *ApJ*, 730, 89, doi: [10.1088/0004-637X/730/2/89](https://doi.org/10.1088/0004-637X/730/2/89)
- Pickles, A., & Depagne, É. 2010, *PASP*, 122, 1437, doi: [10.1086/657947](https://doi.org/10.1086/657947)
- Podsiadlowski, P., Joss, P. C., & Hsu, J. J. L. 1992, *ApJ*, 391, 246, doi: [10.1086/171341](https://doi.org/10.1086/171341)
- Popper, D. M. 1947, *PASP*, 59, 320, doi: [10.1086/125980](https://doi.org/10.1086/125980)
- Rosendhal, J. D., & Schmidt, E. G. 1973, *PASP*, 85, 396, doi: [10.1086/129474](https://doi.org/10.1086/129474)
- Sander, A., Hamann, W. R., & Todt, H. 2012, *A&A*, 540, A144, doi: [10.1051/0004-6361/201117830](https://doi.org/10.1051/0004-6361/201117830)
- Sander, A. A. C., Hamann, W. R., Todt, H., et al. 2019, *A&A*, 621, A92, doi: [10.1051/0004-6361/201833712](https://doi.org/10.1051/0004-6361/201833712)
- Smartt, S. J. 2009, *ARA&A*, 47, 63, doi: [10.1146/annurev-astro-082708-101737](https://doi.org/10.1146/annurev-astro-082708-101737)
- . 2015, *PASA*, 32, e016, doi: [10.1017/pasa.2015.17](https://doi.org/10.1017/pasa.2015.17)

- Smith, L. F. 1968a, MNRAS, 140, 409, doi: [10.1093/mnras/140.4.409](https://doi.org/10.1093/mnras/140.4.409)
- . 1968b, MNRAS, 138, 109, doi: [10.1093/mnras/138.1.109](https://doi.org/10.1093/mnras/138.1.109)
- Smith, N. 2014, ARA&A, 52, 487, doi: [10.1146/annurev-astro-081913-040025](https://doi.org/10.1146/annurev-astro-081913-040025)
- Smith, N., Li, W., Filippenko, A. V., & Chornock, R. 2011, MNRAS, 412, 1522, doi: [10.1111/j.1365-2966.2011.17229.x](https://doi.org/10.1111/j.1365-2966.2011.17229.x)
- Srivastav, S., Anupama, G. C., & Sahu, D. K. 2014, MNRAS, 445, 1932, doi: [10.1093/mnras/stu1878](https://doi.org/10.1093/mnras/stu1878)
- Taddia, F., Sollerman, J., Leloudas, G., et al. 2015, A&A, 574, A60, doi: [10.1051/0004-6361/201423915](https://doi.org/10.1051/0004-6361/201423915)
- Tramper, F., Sana, H., & de Koter, A. 2016, ApJ, 833, 133, doi: [10.3847/1538-4357/833/2/133](https://doi.org/10.3847/1538-4357/833/2/133)
- Tully, R. B., Rizzi, L., Shaya, E. J., et al. 2009, AJ, 138, 323, doi: [10.1088/0004-6256/138/2/323](https://doi.org/10.1088/0004-6256/138/2/323)
- Van Dyk, S. D. 2017, Philosophical Transactions of the Royal Society of London Series A, 375, 20160277, doi: [10.1098/rsta.2016.0277](https://doi.org/10.1098/rsta.2016.0277)
- Van Dyk, S. D., Zheng, W., Brink, T. G., et al. 2018, ApJ, 860, 90, doi: [10.3847/1538-4357/aac32c](https://doi.org/10.3847/1538-4357/aac32c)
- Vanbeveren, D., De Donder, E., Van Bever, J., Van Rensbergen, W., & De Loore, C. 1998, NewA, 3, 443, doi: [10.1016/S1384-1076\(98\)00020-7](https://doi.org/10.1016/S1384-1076(98)00020-7)
- Wellstein, S., & Langer, N. 1999, A&A, 350, 148, <https://arxiv.org/abs/astro-ph/9904256>
- Williamson, M., Kerzendorf, W., & Modjaz, M. 2021, ApJ, 908, 150, doi: [10.3847/1538-4357/abd244](https://doi.org/10.3847/1538-4357/abd244)
- Yoon, S.-C. 2015, PASA, 32, e015, doi: [10.1017/pasa.2015.16](https://doi.org/10.1017/pasa.2015.16)
- . 2017, MNRAS, 470, 3970, doi: [10.1093/mnras/stx1496](https://doi.org/10.1093/mnras/stx1496)
- Yoon, S.-C., Chun, W., Tolstov, A., Blinnikov, S., & Dessart, L. 2019, ApJ, 872, 174, doi: [10.3847/1538-4357/ab0020](https://doi.org/10.3847/1538-4357/ab0020)
- Yoon, S.-C., Dessart, L., & Clocchiatti, A. 2017, ApJ, 840, 10, doi: [10.3847/1538-4357/aa6afe](https://doi.org/10.3847/1538-4357/aa6afe)
- Yoon, S. C., Gräfener, G., Vink, J. S., Kozyreva, A., & Izzard, R. G. 2012, A&A, 544, L11, doi: [10.1051/0004-6361/201219790](https://doi.org/10.1051/0004-6361/201219790)
- Yoon, S. C., Woosley, S. E., & Langer, N. 2010, ApJ, 725, 940, doi: [10.1088/0004-637X/725/1/940](https://doi.org/10.1088/0004-637X/725/1/940)
- Zapartas, E., de Mink, S. E., Van Dyk, S. D., et al. 2017, ApJ, 842, 125, doi: [10.3847/1538-4357/aa7467](https://doi.org/10.3847/1538-4357/aa7467)

APPENDIX

A. OPTICAL MAGNITUDES OF SN Ib/Ic PROGENITORS WITH VARIOUS MASS-LOSS RATES

Table 5. Optical magnitudes of SN Ib/Ic progenitors with various mass-loss rates

Name	<i>HST</i> /WFPC2				<i>HST</i> /WFC3			
	M_{F450W} (mag)	M_{F555W} (mag)	M_{F606W} (mag)	M_{F814W} (mag)	M_{F438W} (mag)	M_{F555W} (mag)	M_{F606W} (mag)	M_{F814W} (mag)
$\dot{M}_{\text{fid}} \times 10.0$								
HE2.91	-5.18	-5.15	-5.18	-5.20	-5.15	-5.13	-5.15	-5.18
HE2.97	-5.42	-5.33	-5.35	-5.32	-5.36	-5.28	-5.28	-5.22
HE4.09	-5.77	-5.75	-5.83	-5.81	-5.37	-5.41	-5.47	-5.58
HE5.05	-6.18	-6.16	-6.24	-6.22	-5.76	-5.80	-5.87	-5.99
CO5.18	-6.59	-6.43	-6.47	-6.54	-6.07	-6.06	-6.08	-6.14
CO5.50	-6.61	-6.39	-6.45	-6.71	-5.90	-5.86	-5.88	-5.92
CO6.17	-6.59	-6.37	-6.41	-6.68	-5.89	-5.85	-5.86	-5.89
CO7.50	-6.51	-6.31	-6.31	-6.52	-5.79	-5.75	-5.76	-5.77
CO9.09	-6.96	-6.95	-6.85	-6.78	-6.08	-6.05	-6.07	-6.11
CO2.16	-4.50	-4.28	-4.30	-4.34	-3.95	-3.91	-3.92	-3.94
CO3.93	-4.28	-4.19	-4.24	-4.33	-3.86	-3.89	-3.94	-4.04
$\dot{M}_{\text{fid}} \times 5.0$								
HE2.91	-5.23	-5.18	-5.19	-5.17	-5.22	-5.18	-5.18	-5.16
HE2.97	-5.39	-5.27	-5.27	-5.18	-5.37	-5.26	-5.23	-5.12
HE4.09	-5.31	-5.22	-5.24	-5.16	-4.99	-4.95	-4.97	-4.99
HE5.05	-5.67	-5.58	-5.61	-5.55	-5.27	-5.28	-5.32	-5.37
CO5.18	-6.12	-5.94	-6.03	-6.25	-5.51	-5.49	-5.51	-5.56
CO5.50	-5.83	-5.62	-5.65	-5.91	-5.14	-5.10	-5.11	-5.14
CO6.17	-5.82	-5.61	-5.63	-5.88	-5.12	-5.08	-5.09	-5.12
CO7.50	-5.80	-5.66	-5.63	-5.76	-5.03	-5.00	-5.01	-5.03
CO9.09	-5.87	-5.80	-5.74	-5.74	-5.01	-4.98	-4.99	-5.02
CO2.16	-3.56	-2.81	-3.60	-3.77	-3.17	-3.15	-3.17	-3.21
CO3.93	-3.77	-2.55	-3.84	-3.97	-3.38	-3.39	-3.42	-3.50
$\dot{M}_{\text{fid}} \times 2.0$								
HE2.91	-5.28	-5.20	-5.21	-5.17	-5.26	-5.21	-5.21	-5.17
HE2.97	-5.08	-4.99	-4.99	-4.94	-5.08	-5.00	-4.99	-4.92
HE4.09	-4.86	-4.68	-4.65	-4.52	-4.73	-4.59	-4.56	-4.44
HE5.05	-4.92	-4.78	-4.76	-4.75	-4.65	-4.62	-4.63	-4.65
CO5.18	-5.34	-5.20	-5.23	-5.42	-4.74	-4.72	-4.74	-4.77
CO5.50	-5.09	-5.03	-4.99	-5.03	-4.33	-4.30	-4.32	-4.37

Table 5 *continued*

Table 5 (continued)

Name	<i>HST</i> /WFPC2				<i>HST</i> /WFC3			
	M_{F450W} (mag)	M_{F555W} (mag)	M_{F606W} (mag)	M_{F814W} (mag)	M_{F438W} (mag)	M_{F555W} (mag)	M_{F606W} (mag)	M_{F814W} (mag)
CO6.17	-5.10	-5.07	-5.01	-4.98	-4.30	-4.28	-4.30	-4.34
CO7.50	-5.10	-5.08	-4.92	-4.85	-4.17	-4.15	-4.17	-4.22
CO9.09	-5.12	-5.02	-4.80	-4.78	-4.13	-4.11	-4.13	-4.19
CO2.16	-3.22	-3.16	-3.13	-3.14	-2.56	-2.54	-2.55	-2.58
CO3.93	-3.33	-3.18	-3.22	-3.42	-2.80	-2.78	-2.80	-2.83
$\dot{M}_{\text{fid}} \times 1.0$								
HE2.91	-5.26	-5.19	-5.19	-5.16	-5.25	-5.20	-5.20	-5.15
HE2.97	-5.11	-5.01	-5.00	-4.92	-5.12	-5.03	-5.01	-4.91
HE4.09	-4.73	-4.54	-4.48	-4.31	-4.67	-4.50	-4.46	-4.26
HE5.05	-4.56	-4.39	-4.34	-4.29	-4.37	-4.27	-4.25	-4.20
CO5.18	-4.83	-4.84	-4.76	-4.74	-4.13	-4.12	-4.15	-4.21
CO5.50	-4.54	-4.42	-4.24	-4.27	-3.69	-3.68	-3.70	-3.77
CO6.17	-4.59	-4.46	-4.22	-4.22	-3.67	-3.66	-3.68	-3.75
CO7.50	-4.53	-4.52	-4.25	-4.11	-3.51	-3.51	-3.54	-3.63
CO9.09	-4.42	-4.39	-4.10	-3.97	-3.35	-3.34	-3.37	-3.45
CO2.16	-2.66	-2.55	-2.40	-2.45	-1.92	-1.91	-1.94	-2.00
CO3.93	-2.83	-2.81	-2.78	-2.78	-2.22	-2.21	-2.24	-2.30
$\dot{M}_{\text{fid}} \times 0.5$								
HE2.91	-5.29	-5.22	-5.22	-5.17	-5.29	-5.23	-5.23	-5.17
HE2.97	-5.05	-4.95	-4.94	-4.88	-5.05	-4.97	-4.96	-4.87
HE4.09	-4.89	-4.68	-4.60	-4.41	-4.85	-4.66	-4.61	-4.37
HE5.05	-4.39	-4.18	-4.12	-4.00	-4.24	-4.09	-4.05	-3.91
CO5.18	-4.33	-4.20	-3.94	-3.95	-34.6	-3.45	-3.49	-3.57
CO5.50	-3.84	-3.89	-3.68	-3.53	-3.01	-2.99	-3.02	-3.10
CO6.17	-3.77	-4.03	-3.86	-3.54	-2.98	-2.97	-3.00	-3.10
CO7.50	-3.31	-3.38	-3.28	-3.30	-2.80	-2.81	-2.85	-2.98
CO9.09	-3.24	-3.17	-3.08	-3.19	-2.72	-2.73	-2.77	-2.90
CO2.16	-1.91	-2.05	-1.89	-1.73	-1.20	-1.20	-1.23	-1.32
CO3.93	-2.33	-2.19	-2.01	-2.04	-1.65	-1.63	-1.65	-1.72
$\dot{M}_{\text{fid}} \times 0.1$								
HE2.91	-5.28	-5.21	-5.20	-5.16	-5.28	-5.22	-5.21	-5.16
HE2.97	-5.06	-4.96	-4.95	-4.87	-5.06	-4.98	-4.96	-4.87
HE4.09	-4.86	-4.64	-4.57	-4.34	-4.87	-4.66	-4.60	-4.31
HE5.05	-4.34	-4.10	-4.03	-3.79	-4.33	-4.11	-4.04	-3.74
CO5.18	-2.68	-2.92	-2.08	-2.35	-2.37	-2.21	-2.17	-2.06
CO5.50	-2.16	-2.01	-1.91	-1.85	-1.91	-1.75	-1.72	-1.63
CO6.17	-2.04	-1.85	-1.75	-1.75	-1.71	-1.58	-1.56	-1.52
CO7.50	-1.57	-1.42	-1.36	-1.39	-1.37	-1.27	-1.27	-1.27

Table 5 continued

Table 5 (*continued*)

Name	<i>HST</i> /WFPC2				<i>HST</i> /WFC3			
	M_{F450W} (mag)	M_{F555W} (mag)	M_{F606W} (mag)	M_{F814W} (mag)	M_{F438W} (mag)	M_{F555W} (mag)	M_{F606W} (mag)	M_{F814W} (mag)
CO9.09	-1.43	-1.30	-1.25	-1.26	-1.31	-1.20	-1.20	-1.19
CO2.16	0.52	0.57	0.61	0.51	0.73	0.75	0.72	0.61
CO3.93	-1.11	-1.31	-1.19	-0.65	-0.87	-0.67	-0.62	-0.43

NOTE—The meaning of each model name is same as that in Table 1. The absolute magnitudes in *HST*/WFPC2 and *HST*/WFC3 filters are presented under the various mass-loss rate assumptions. \dot{M}_{fid} denotes the fiducial mass-loss rate in this study.

B. NORMALIZED OPTICAL SPECTRA OF FIDUCIAL MODELS

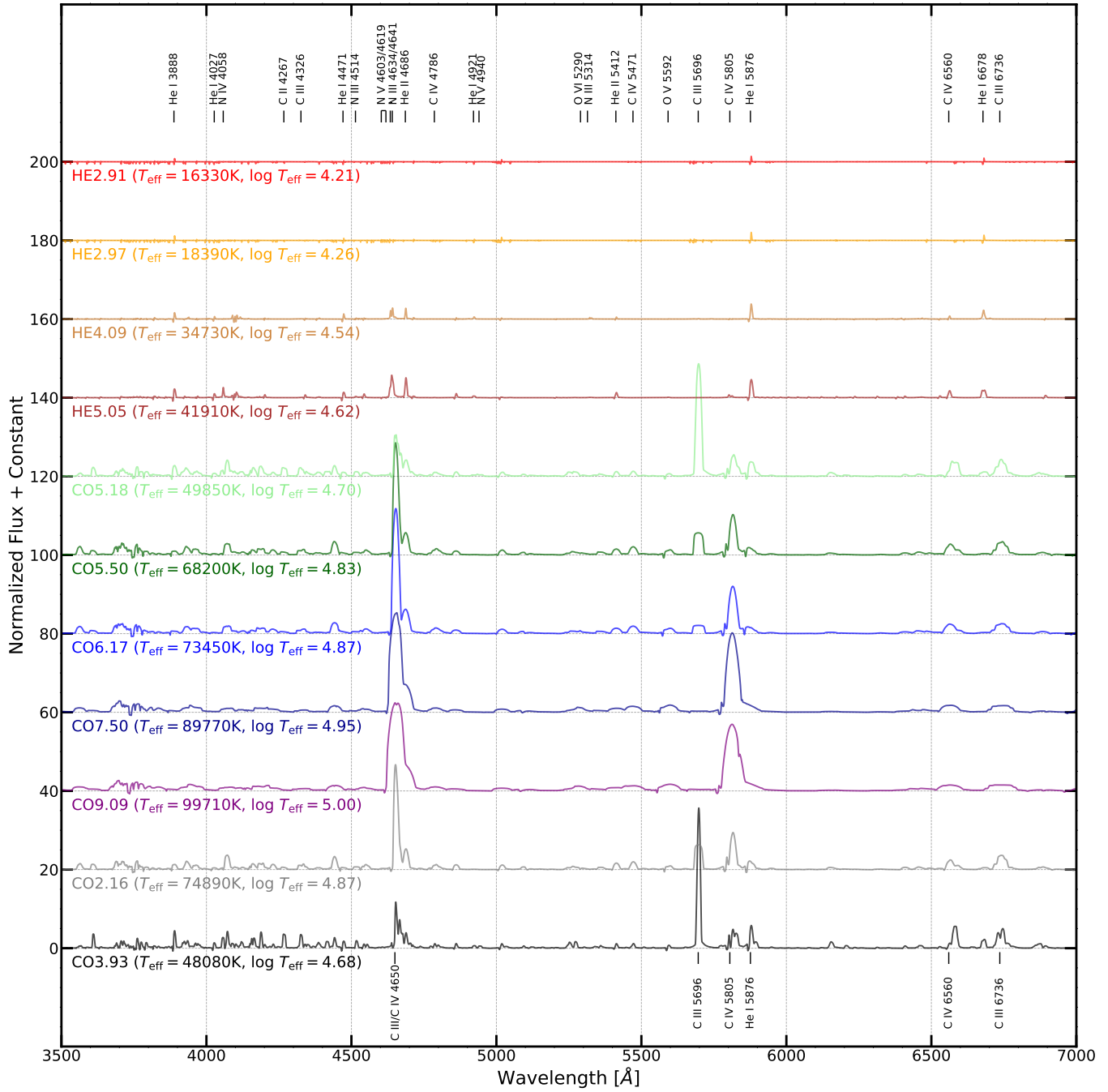


Figure 13. Normalized spectra of fiducial SN Ib/Ic progenitor models in the wavelength ranges $3500\text{Å} \leq \lambda \leq 7000\text{Å}$, which correspond to the $F435W$ and $F555W$ filter range.

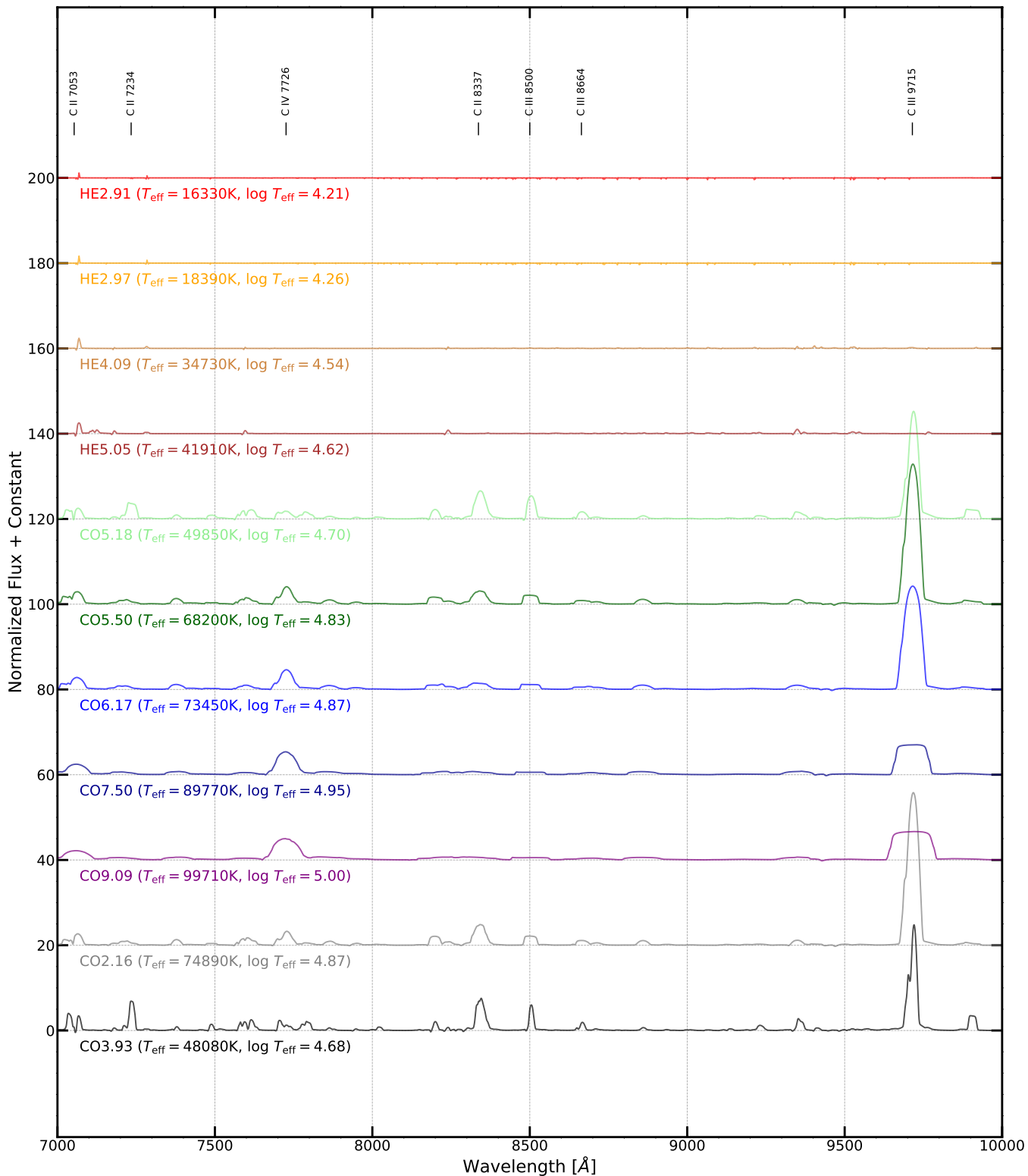


Figure 14. Normalized spectra of fiducial SN Ib/Ic progenitor models in the wavelength ranges $7000\text{\AA} \leq \lambda \leq 10000\text{\AA}$, which correspond to the $F814W$ filter range.

C. CHANGE OF SPECTRA ACCORDING TO VARIOUS MASS-LOSS RATES

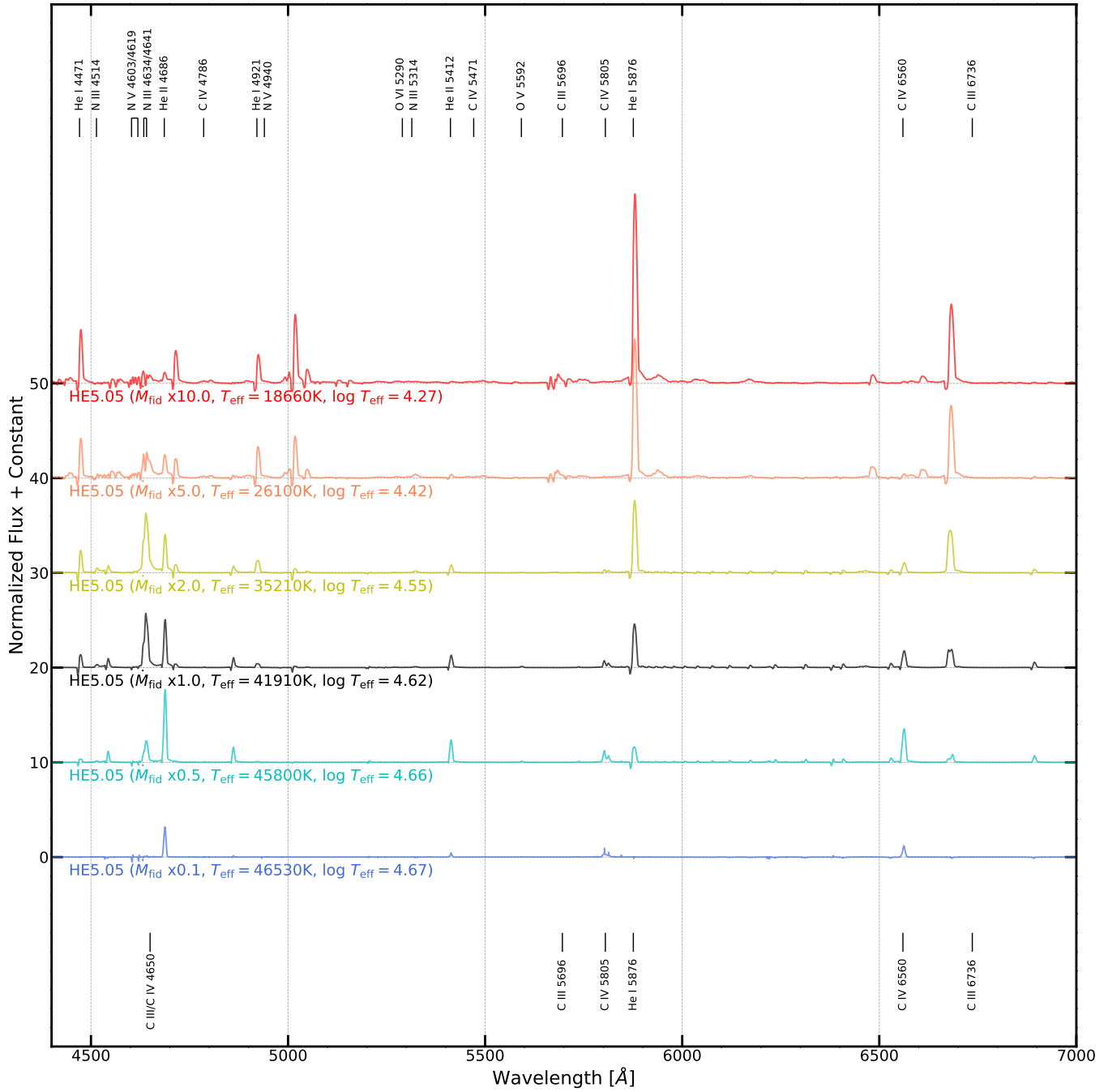


Figure 15. Normalized spectra of HE5.05 model with various mass-loss rates. Spectra are presented in the wavelength ranges $4400 \text{ \AA} \leq \lambda \leq 7000 \text{ \AA}$, which correspond to the wavelength range of the $F555W$ filter.

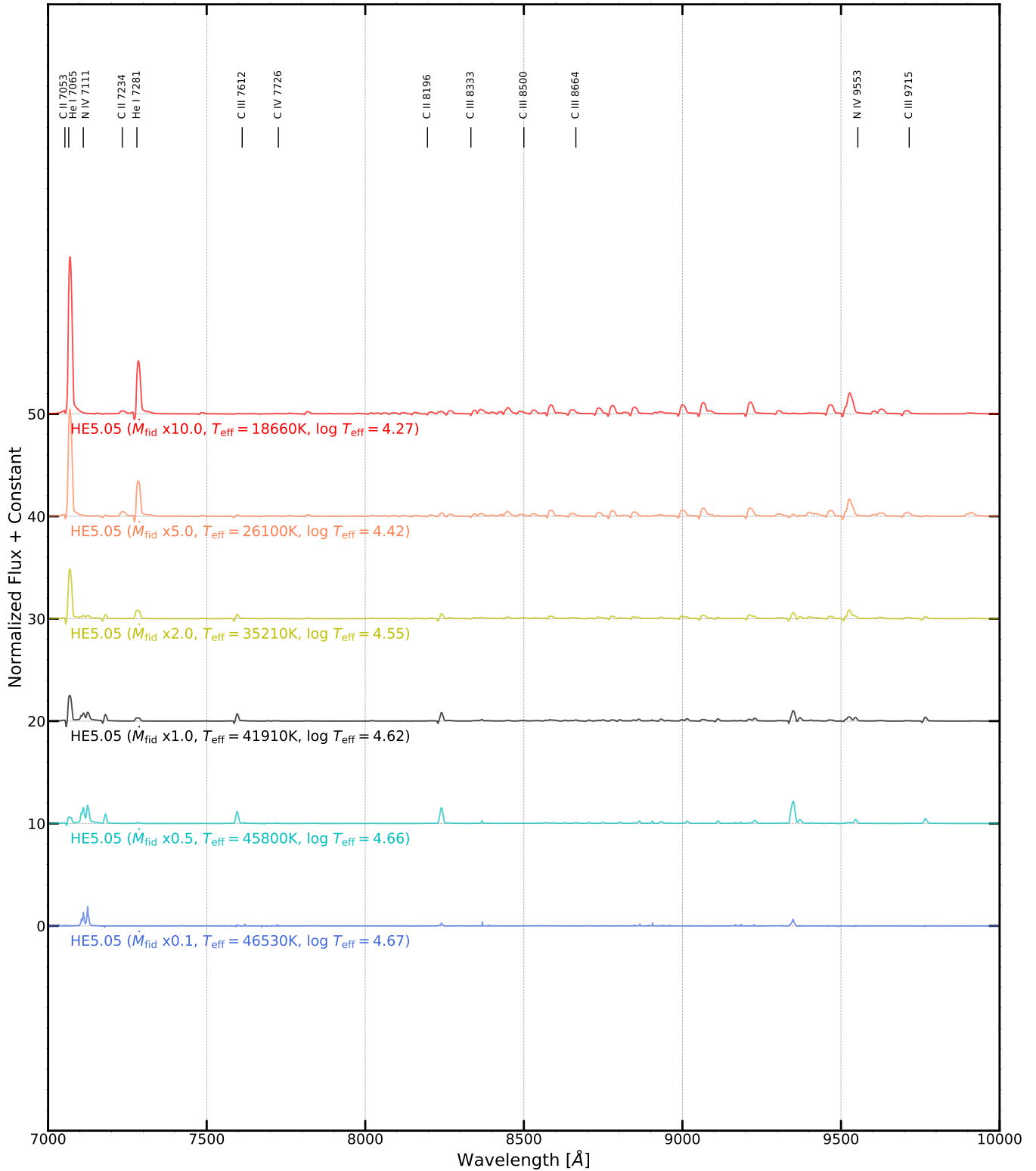


Figure 16. Normalized spectra of HE5.05 model with various mass-loss rates. Spectra are presented in the wavelength ranges $7000 \text{ \AA} \leq \lambda \leq 10000 \text{ \AA}$, which correspond to the wavelength range of the $F814W$ filter.

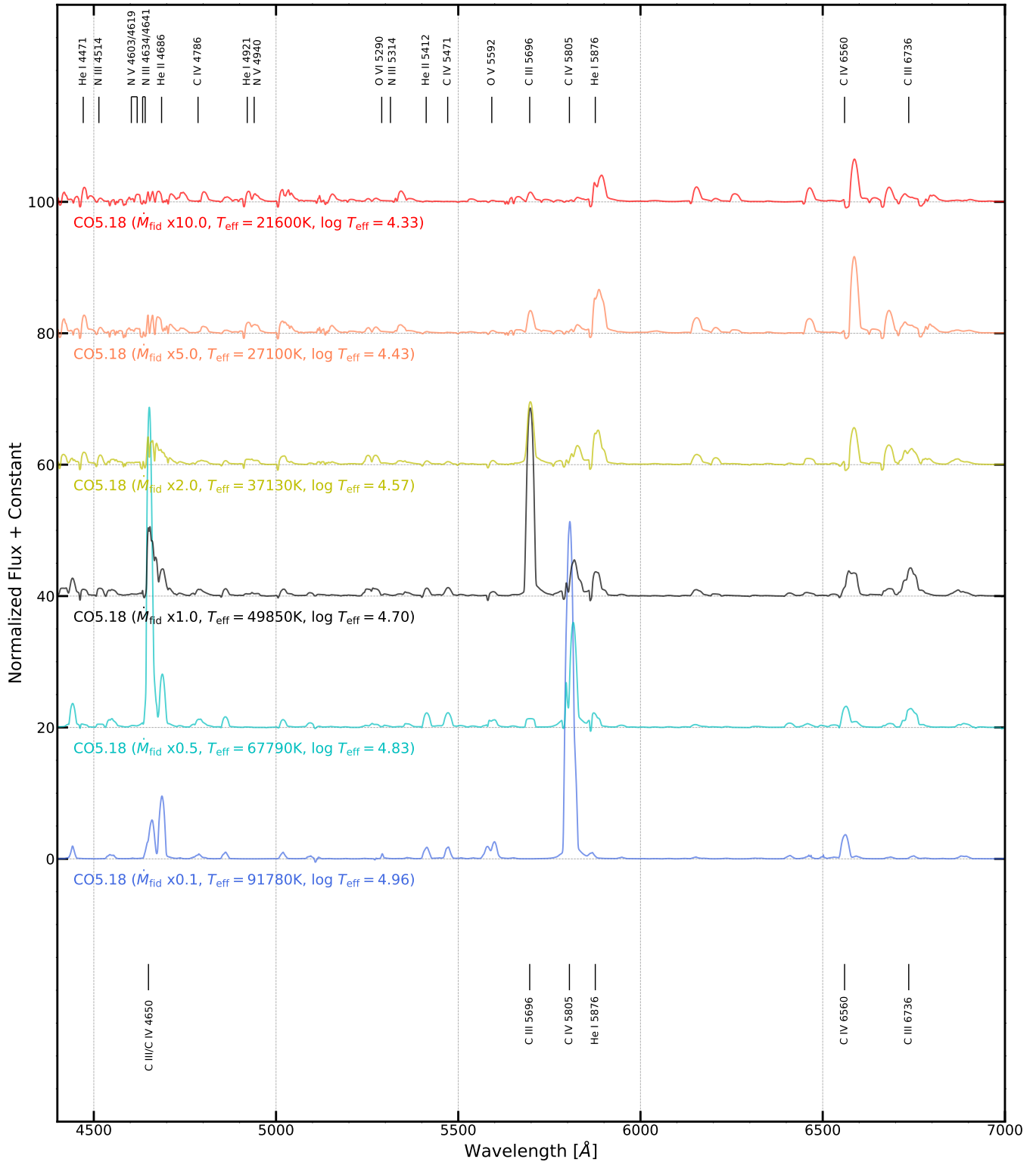


Figure 17. Normalized spectra of CO5.18 model with various mass-loss rates. Spectra are presented in the wavelength ranges $4400 \text{ \AA} \leq \lambda \leq 7000 \text{ \AA}$, which correspond to the wavelength range of the $F555W$ filter.

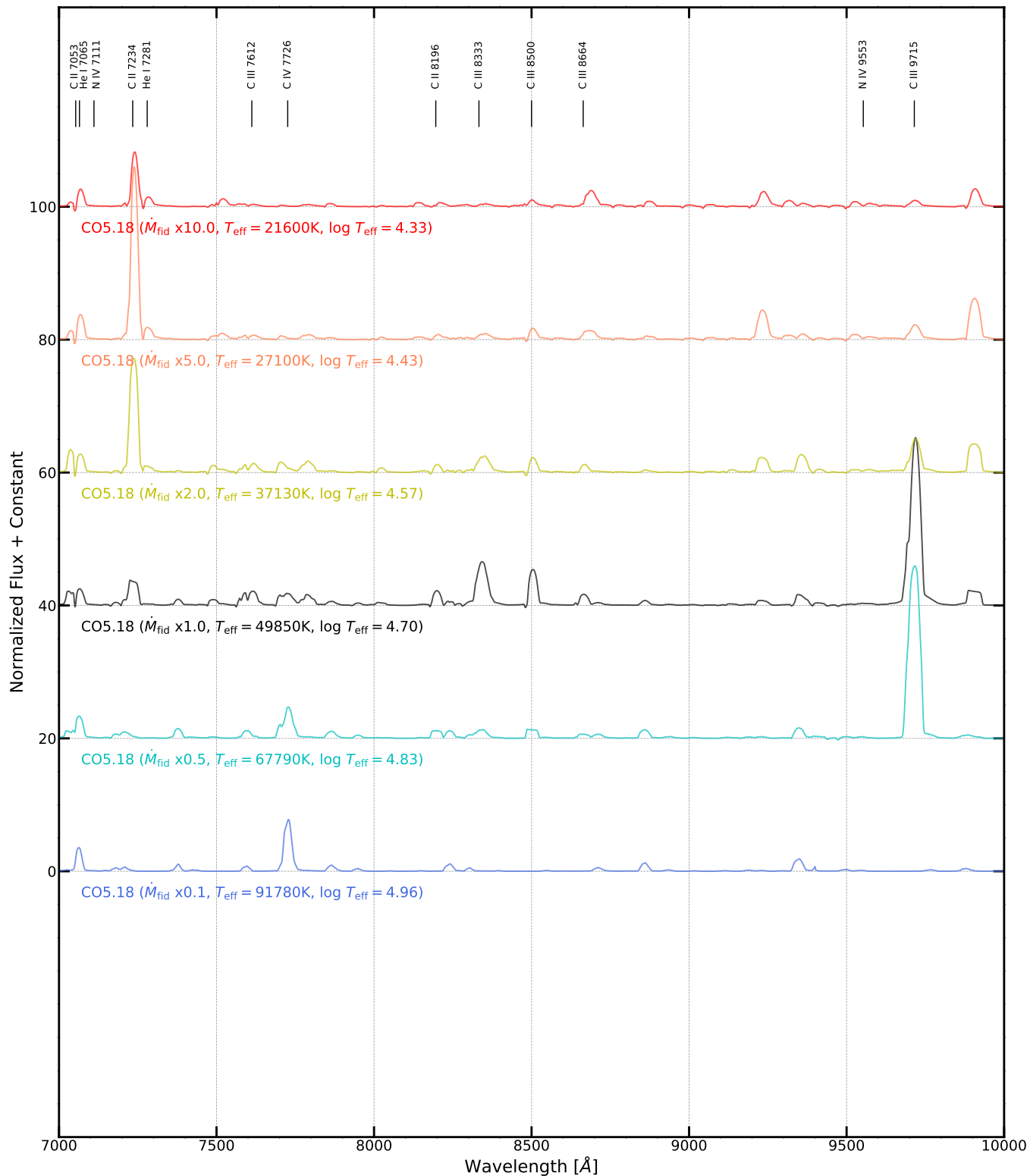


Figure 18. Normalized spectra of CO5.18 model with various mass-loss rates. Spectra are presented in the wavelength ranges $7000 \text{ \AA} \leq \lambda \leq 10000 \text{ \AA}$, which correspond to the wavelength range of the *F814W* filter.